DEPARTMENT OF PHYSICS
UNIVERSITY OF JYVÄSKYLÄ

LIGHT COUPLING INTO PLANAR DIELECTRIC WAVEGUIDE BY PLASMONIC NANOPARTICLES

BY
ANTTI PENNANEN

Thesis for the Degree of
Licentiate of Philosophy

Jyväskylä, Finland
October 2013

Preface

The work presented in this thesis was conducted at the Nanoscience Center and Department of Physics at the University of Jyväskylä in 2009–2013. The research project was funded by Foundation for Research of Natural Resources in Finland (Suomen Luonnonvarain Tutkimussäätiö), for which I wish to express my gratitude. I wish to thank my supervisor, Doc. Jussi Toppari, my fellow graduate students and the laboratory engineers at the Nanoscience Center for all the guidance, conversations, advice and help. I address special thanks to Holvi, for the caring atmosphere and inspiration, and to Ropeapina, for putting my mind off the work. Especially warm thanks goes to my parents and to my sister for all the support they have given me during all of my life.

Jyväskylä, June 2013

Antti Pennanen

Abstract

In this thesis work, a concept of window integrated solar concentrator, that takes advantage of light coupling into a planar dielectric waveguide via localized surface plasmons (LSP) on metallic nanoparticles was investigated. Different methods for nanoparticle fabrication were examined for the purpose of producing particles that have localized surface plasmon resonance (LSPR) just beyond the wavelength of visible light. Particles were characterized by means of transmittance spectroscopy. Most importantly, a method and setup for direct optical measurements of the coupling of light into a planar waveguide by plasmonic nanoparticles was developed, in order to study the efficiency of the proposed window integrated solar consentrator. Samples consisting of Au nanodisks deposited either on plain 1 mm thick glass slides or glass slides coated with high-refractive-index dielectric material were fabricated for the measurements. While the light coupling into the waveguide by the particle plasmons was succesfully detected by the direct optical measurement, it was also found out that, due to a waveguide-mediated effect, the nanoparticles also very strongly absorb the in-coupled light. This presents a fundamental obstacle for the current window integrated solar consentrator design based on plasmonic nanoparticles.

Contents

1 Introduction **1**

2 Theory and background **3**
2.1 Plasmons 3
2.1.1 Bulk plasmons in classical theory of solids 4
2.1.2 Plasma frequency and dielectric function of a Drude metal 5
2.1.3 Localized surface plasmons 7
2.2 Dielectric slab waveguide 9
2.2.1 Electromagnetic equations for the dielectric slab waveguide 9
2.2.2 Dispersion relations of the TE and TM modes 12
2.2.3 Field profiles 13
2.3 Plasmon enhanced thin-film solar cells 15
2.4 Window glass integrated solar concentrator 17

3 Experimental **19**
3.1 Sample fabrication and characterization 20
3.1.1 Metal island film evaporation 21
3.1.2 Hole-mask colloidal lithography 24
3.2 Results and discussion 25
3.2.1 Emission measurements 25
3.2.2 Integrating sphere measurements 31
3.2.3 Emission measurements on ellipsoidal nanoparticles . . . 33

4 Conclusions **38**

References **40**

A Included publication **45**

1

Introduction

Metallic nanoparticles support localized surface plasmon (LSP) modes, *i.e.* collective oscillations of the delocalized conduction electrons, induced by electromagnetic (EM) radiation. In analogy to a damped mechanical oscillator, the amplitude of the electron plasma oscillation may become very large when a periodic driving force is applied at a certain resonant frequency. For metallic nanoparticles, this frequency of localized surface plasmon resonance (LSPR) lies within range of visible to near-infrared light. The resonant oscillations give rise to high cross sections for scattering and absorption of light, compared to the geometrical size of the particle, and strong, highly localized fields close to the particle. Because of this property, plasmonic nanoparticles have attracted considerable attention in applications such as biological sensing and tagging [1, 2], surface enhanced Raman spectroscopy (SERS) [3], and subwavelength photonic components [4, 5], among others.

Most relevant to the interests of this thesis, however, is the application of plasmonic nanoparticles in solar energy conversion. There are two fundamental phenomena which may allow plasmonic nanoparticles to enhance the performance of solar cells [6]: (i) enhanced charge carrier generation by the strong near electric fields of the localized surface plasmons on nanoparticles embedded in photovoltaic material, and (ii) light trapping by scattering from LSPs on particles located on the front or rear surface of a solar cell. To exploit the former mechanism (i), the nanoparticles should be embedded into the active layer of the solar cell, where the increased intensity of the electric fields localized near the plasmonic particle, which may be orders of magnitude larger than the intensity of the field of the incident radiation, leads to enhanced charge carrier generation. In the latter case (ii), light scattered by the nanoparticles is trapped within the

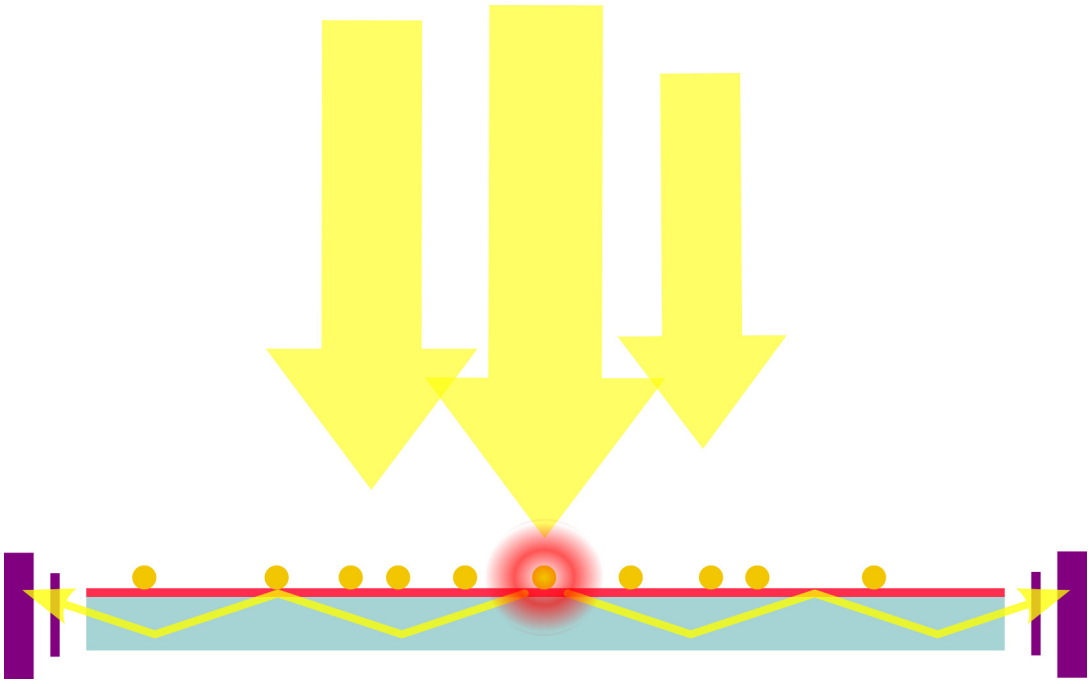

Figure 1.1: The operating principle of proposed window integrated solar concentrator.

active layer of the cell in such a way that the average optical path length of photons is greatly enhanced, resulting in enhanced energy conversion efficiency. In the scope of the work presented in this thesis, the latter mechanism is the one of significance.

The original purpose of the work presented in this thesis was to develop a window integrated solar concentrator, that would utilize coupling of light, via LSPs on metallic nanoparticles, to the guided electromagnetic modes in planar dielectric waveguide (see Fig. 1.1). The proposed operating principle was that nanoparticles located on the front or rear surface of the glass would scatter incident light into the glass pane, or a separate transparent high refractive index waveguide layer deposited on the glass. The radiation coupled into the glass, or the separate waveguide layer, would then propagate to the edges of the glass pane, where the electromagnetic energy could be collected and converted into some usable form.

2

Theory and background

In this chapter, some basic theory of plasmons and planar waveguides is presented, to the extent that is necessary in order to understand the experimental part of this thesis. The bulk plasmon is described in terms of classical theory of solids, as an introduction to the localized surface plasmons on metallic nanoparticles. The basic electromagnetic equations of planar dielectric waveguides are presented and the dispersion relations for the transverse electric (TE) and magnetic (TM) modes are derived. Properties of plasmonic nanoparticles and planar dielectric waveguides relate to the plasmon enhanced solar cells, from which the proposed window integrated solar concentrator concept is partially derived.

2.1 Plasmons

Plasmon is the quantization of collective oscillations of delocalized conduction electrons in metals, induced by time-harmonic electric field. However, the existence of these collective electron plasma oscillations may be demonstrated by a purely classical treatment. Inside a perfect conductor the net electric field is always zero, and propagation of electromagnetic waves is not permitted. This arises from the free conduction electrons that, under external electric field, are collectively deflected with respect to the metal lattice composed of positively charged nucleai, to negate the field inside the conductor. In real metals however, the electrons experience damping due to inertia, electron-electron collisions and interactions with lattice ions. If the oscillation of the external electric field is faster than the characteristic relaxation time, then the electrons are not able to keep in phase, and at sufficiently large frequency, electromagnetic wave propaga-

tion becomes allowed. This is the reason behind the ultraviolet transparency of the free-electron type metals [7]. The limiting frequency, above which the wave propagation becomes allowed, is called the plasma frequency. Below the plasma frequency the electric field decays exponentially in space, with the skin depth approaching zero at the DC limit. At the plasma frequency, a metal exhibits sustained collective oscillation of its electrons. Bulk plasmon is the quantization of this oscillation of conduction electron plasma. Presence of interfaces alters the nature of the plasma oscillation. Plasmons at planar interfaces between metal and insulator, *i.e.* surface plasmon polaritons (SPP) are restricted into two dimensions, and plasmons in small particles are called localized surface plasmons (LSP).

2.1.1 Bulk plasmons in classical theory of solids

The response of the electrons of a metal to an external time-harmonic electric field may be described with a frequency dependent dielectric function $\varepsilon(\omega)$. From Maxwell's equations one may obtain an inhomogeneous wave equation for the time-dependent electric field $\mathbf{E}$ in a medium with conductivity σ:

$$\nabla^2\mathbf{E} = \mu_0\sigma\frac{\partial\mathbf{E}}{\partial t} + \mu_0\varepsilon_0\frac{\partial^2\mathbf{E}}{\partial t^2}, \tag{2.1}$$

where μ_0 and ε_0 are the magnetic permeability and dielectric permittivity of vacuum, respectively. By assuming a sinusoidal electric field $\mathbf{E} = \mathbf{E}(\mathbf{r},\omega)\exp(-i\omega t)$ this becomes something formally resembling a wave-equation,

$$\nabla^2\mathbf{E}(\mathbf{r},\omega) = -\frac{\omega^2}{c^2}\varepsilon(\omega)\mathbf{E}(\mathbf{r},\omega), \tag{2.2}$$

where we have defined the frequency dependent dielectric function as

$$\varepsilon(\omega) = 1 + \frac{i\sigma(\omega)}{\omega\varepsilon_0}. \tag{2.3}$$

In case of a positive and real $\varepsilon(\omega)$, the solutions to the equation (2.2) are of form $\mathbf{E}(\mathbf{r},\omega) = \mathbf{E}(\omega)\exp(i\mathbf{k}\cdot\mathbf{r}))$, *i.e.* plane waves with wave-vector $\mathbf{k}$. With a negative and real $\varepsilon(\omega)$ solutions are exponentially decaying in space, *i.e.* of form $\mathbf{E}(\omega,\mathbf{r}) = \mathbf{E}(\omega)\exp(-\alpha r)$, where the attenuation constant α is real. The transition from the conducting to insulating behaviour occurs at $\varepsilon(\omega) = 0$, and we shall shortly see that this corresponds to sustained electron plasma oscillation in the metal at the plasma frequency.

In classical theory of solids, the existence of sustained charge density oscillations may be observed by looking for time harmonic solutions of the continuity equation for the charge density ρ [8, pp.1–27]

$$\nabla \cdot \mathbf{j} + \frac{\partial \rho}{\partial t} = 0, \tag{2.4}$$

where $\mathbf{j}$ denotes the current density. Using a trial $\rho = \rho(\omega)\exp(-i\omega t)$ the continuity equation (2.4) becomes

$$\nabla \cdot \mathbf{j}(\omega) = i\omega\rho(\omega). \tag{2.5}$$

By using the Ohm's law $\mathbf{j}(\omega) = \sigma(\omega)\mathbf{E}(\omega)$ and Maxwell's equation $\nabla \cdot \mathbf{E} = \frac{\rho}{\varepsilon_0}$ one may express the divergence of the current density as

$$\nabla \cdot \mathbf{j}(\omega) = \frac{\sigma(\omega)\rho(\omega)}{\varepsilon_0}. \tag{2.6}$$

Setting expressions (2.5) and (2.6) equal leads to the condition

$$\varepsilon(\omega) = 1 + \frac{i\sigma(\omega)}{\omega\varepsilon_0} = 0, \tag{2.7}$$

as mentioned earlier. This means that the sustained electron plasma oscillation occurs at frequencies where the dielectric function of the medium is zero.

2.1.2 Plasma frequency and dielectric function of a Drude metal

The simplest classical model for electronic behaviour of metals is the Drude model. In Drude model, the electrons of a metal are considered as a free electron gas, *i.e.* there are no interactions between the electrons and ions of the metallic lattice, and the response of the electrons to an external electric field is damped only by inertia. From the equation of motion for momentum $\mathbf{p}$ per electron in a free-electron gas [8, pp.1–27]

$$\frac{d\mathbf{p}(t)}{dt} + \frac{\mathbf{p}(t)}{\tau} + e\mathbf{E} = 0, \tag{2.8}$$

where τ is the electronic relaxation time, *i.e.* the average time between two subsequent collisions of electrons, and by using a trial $\mathbf{p}(t) = \mathbf{p}(\omega)\exp(-i\omega t)$ for the single electron momentum under a sinusoidal electric field $\mathbf{E}(t) = \mathbf{E}(\omega)\exp(i\omega t)$, and $\mathbf{j} = -ne\mathbf{v} = \sigma\mathbf{E}$ one acquires the Drude model expression for AC-conductivity

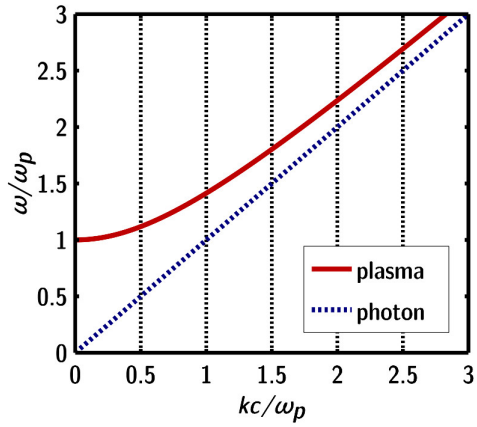

Figure 2.1: Dispersion relation of the free-electron gas (Drude metal), together with the dispersion of light (photon). The plasma frequency is denoted with ω_p.

$$\sigma(\omega) = \frac{ne^2\tau}{m(1 - i\omega\tau)}, \tag{2.9}$$

where n denotes the electron density. Substituting this to the condition for the sustained plasma oscillation (2.7) one obtains

$$\varepsilon(\omega) = 1 + \frac{ne^2}{m\varepsilon_0}\left(\frac{i\tau}{\omega(1 - i\omega\tau)}\right) = 0. \tag{2.10}$$

This condition is fulfilled if $\omega\tau \gg 1$ and

$$\boxed{\omega = \sqrt{\frac{ne^2}{m\varepsilon_0}} \equiv \omega_p,} \tag{2.11}$$

where we have defined the plasma frequency ω_p for the collective oscillation of the electron plasma. Using the definition of the plasma frequency for Drude metal one may write the complex, frequency dependent dielectric function as

$$\boxed{\varepsilon(\omega) = 1 - \frac{\omega_p^2}{\omega^2 + i\frac{1}{\tau}\omega}.} \tag{2.12}$$

At the limit of high frequency, $\omega\tau \gg 1$ and $\omega \geq \omega_p$ the dielectric function is positive and real, and thus the solutions to the "wavelike" equation (2.2) are plane waves, *i.e.* Drude metal becomes transparent to EM radiation. Inserting

the plane wave ansatz and the dispersion relation at high frequency limit into eq. (2.2) yields the dispersion relation of free-electron plasma,

$$\omega^2 = \mathbf{k}^2 c^2 + \omega_p^2, \qquad \omega \geq \omega_p, \tag{2.13}$$

which is illustrated in Fig. 2.1, and where c is the speed of light in vacuum. At the low-frequency limit $\varepsilon(\omega)$ approaches negative infinity, totally denying penetration of any electric field into the metal, and free-electron metal becomes a perfect conductor.

2.1.3 Localized surface plasmons

Interfaces present boundary conditions to the electromagnetic equations. The geometry of the problem at hand defines the boundary conditions which in turn lead to different solutions to the EM equations. Different geometries thus give rise to different kinds of plasmons.

It can be shown [9, pp.21–37] [10, pp.369–413] that at a plane interface between a metal and an insulator the wave equation (2.2) has solutions that are evanescent in direction perpendicular to the interface and propagating in the parallel direction. These solutions represent the so-called surface plasmon polaritons (SPP), *i.e.* propagating surface charge oscillations. The dispersion relation of the SPP is such that the wavenumber of an SPP is always larger than the wavenumber of light of the same frequency (energy). Thus, due to the requirement for conservation of energy and momentum, it is not possible for an SPP to decay into or be excited by free-space radiation, unless some surface defect is introduced or a special geometry for excitation is arranged.

Other geometries that allow analytical treatment are nanospheres and nanowires with circular cross-section. Metallic nanowires support propagating plasmonic modes along the length of the wire (longitudinal modes), similar to the plasmons on planar interfaces, but also standing, transverse modes [10]. The principal transverse mode is a dipole mode, which has the electron plasma of the metal nanowire oscillating collectively in phase, in the direction perpendicular to the length of the wire. At higher energies, excitation of higher order modes becomes possible. The plasmonic modes of metallic nanospheres are similar to the transverse modes of nanowires with a circular cross section. These transverse, non-propagating modes are called localized surface plasmons (LSP). The electric field distribution associated with a dipolar plasmonic mode of a metallic nanoparticle is depicted in Fig. 2.2. Contrary to the surface plasmon polaritons, LSPs may be excited directly by free-space light. In nanowires, the transverse oscillations can only be induced by radiation that has electric field component

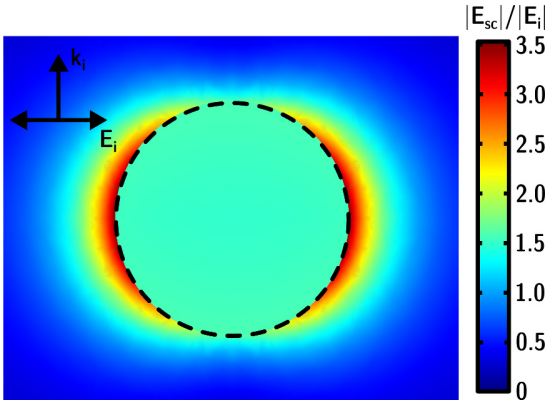

Figure 2.2: The scattered electric field amplitude $|\mathbf{E}_{sc}|$ by a 40 nm diameter gold nanosphere in air ((total field) − (incident field)), when the wavelength of the incident plane-wave is 510 nm. Incident wave-vector and electric field are denoted with $\mathbf{k}_i$ and $\mathbf{E}$, respectively. Simulated with COMSOL, dielectric function for gold interpolated from data of Johnson and Christy [11].

in direction perpendicular to the length of the wire, whereas LSPs on metal nanospheres may be excited from arbitrary direction. Occurence of LSPs is of course not limited to aforementioned geometries, but all shapes of particles or structures with sufficiently small dimensions support localized plasmons.

Unlike the SPPs or the propagating longitudinal modes, the transverse LSP modes can only have certain resonance wavelengths/frequencies. Strong scattering and absorption are associated with these resonances. The radiative part of the electromagnetic field of the LSP constitutes the scattering and the non-radiative near-field, decaying exponentially in distance, accounts for the absorption. Beyond the so called quasistatic treatment of localized surface plasmons, there is also the effect of plasmon lifetime and damping via radiative decay or electron-hole generation [9, pp.65–88] [12]. Electron-hole excitations manifest as particle heating and add to the absorption loss.

The LSP resonance (LSPR) frequency is determined by the particle material (dielectric function), size, shape and the dielectric environment of the particle. Metallic particles with larger diameter have their LSP resonance on lower frequency (longer wavelength) than those with smaller diameter, and their extinction is dominated by scattering (over absorption), *i.e.* they have larger scattering efficiency. Larger particles are thus preferable to smaller ones for the waveguide coupling application considered in this thesis. Under free-space electromagnetic radiation the LSPR frequency is lower (longer wavelength) if the particle shape

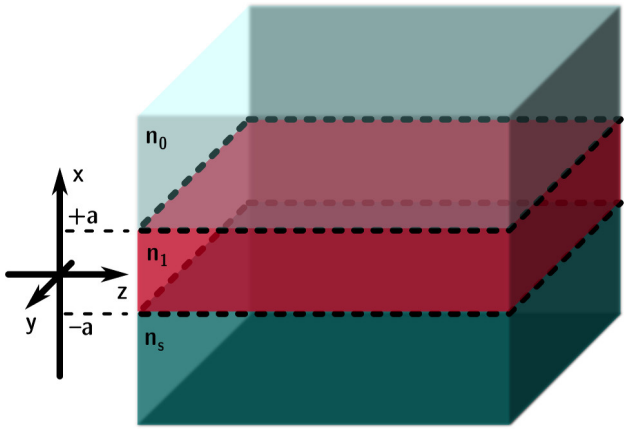

Figure 2.3: Dielectric slab waveguide. For guided modes to exist, refractive indices must satisfy $n_1 > n_0, n_s$.

is more flat in the direction of wave propagation, *i.e.* if the dimension of the particle is shorter in that direction. The effect of dielectric substrate and/or overcoating is to shift the resonance to lower frequency (longer wavelength); the higher the dielectric constant (and refractive index), the larger the shift (see Fig. 3.5 in Chapter 3.1.1 for an example).

2.2 Dielectric slab waveguide

A dielectric slab waveguide is formed of two planar interfaces, separating three semi-infinite regions of space with different indices of refraction, as depicted in Fig. 2.3. The three regions are called the cladding, core and substrate, with refractive indices n_0, n_1 and n_s, respectively. In order to have guided wave propagation within the core, the dielectric indices have to satisfy $n_1 > n_0, n_s$ [13, pp.1–27]. In the case of thin-film solar cells the core may be crystalline silicon on oxidized silicon substrate and with the glass cover as the cladding.

2.2.1 Electromagnetic equations for the dielectric slab waveguide

Dispersion relations for guided modes of such a waveguide are obtained by solving the electromagnetic equations for the dielectric slab waveguide. These are obtained from Maxwell's equations, wich one may write in this case as

$$\nabla \times \mathbf{E} = -\mu_0 \frac{\partial \mathbf{H}}{\partial t}, \tag{2.14a}$$

$$\nabla \times \mathbf{H} = n^2 \varepsilon_0 \frac{\partial \mathbf{E}}{\partial t}, \tag{2.14b}$$

where n is the refractive index. We are looking for solutions that depict modes within the slab waveguide, propagating in direction along the slab, *i.e.* in z-direction (see Fig. 2.3):

$$\mathbf{E} = \mathbf{E}_0(x) e^{i(\omega t - \beta z)}, \tag{2.15a}$$

$$\mathbf{H} = \mathbf{H}_0(x) e^{i(\omega t - \beta z)}, \tag{2.15b}$$

where $\beta = n_1 k_{0,z}$ is called the propagation constant (*i.e.* the wave vector component in direction of the guided wave propagation in the core of the waveguide), and where $k_{0,z}$ denotes the z-component of the wave vector corresponding to a vacuum plane wave with the same energy. Note that we do not limit the trial solutions to transverse electromagnetic waves, but allow the fields to also have a component along the direction of propagation. Substituting these ansätze into the Maxwell's equations yields two sets of equations:

$$-i\omega\mu_0 H_x = i\beta E_y, \tag{2.16a}$$

$$-i\omega\mu_0 H_y = -\frac{\partial E_z}{\partial x} - i\beta E_x, \tag{2.16b}$$

$$-i\omega\mu_0 H_z = \frac{\partial E_y}{\partial x}, \tag{2.16c}$$

and

$$i\omega n^2 \varepsilon_0 E_x = i\beta H_y, \tag{2.17a}$$

$$i\omega n^2 \varepsilon_0 E_y = -\frac{\partial H_z}{\partial x} - i\beta H_x, \tag{2.17b}$$

$$i\omega n^2 \varepsilon_0 E_z = \frac{\partial H_y}{\partial x}, \tag{2.17c}$$

where we have used the fact that $\mathbf{E}$ and $\mathbf{H}$ only depend on x and not y, so that the partial derivatives of the field with respect to y are zero. One may then express H_x and H_z in terms of E_y, and E_x and E_z in terms of H_y, to obtain two independent sets of equations:

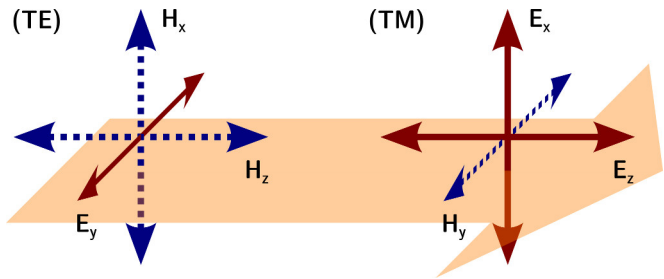

Figure 2.4: Electric and magnetic field components of TE and TM modes in a dielectric slab waveguide.

$$
\text{(TE)} \begin{cases}
\dfrac{\partial^2 E_y}{\partial x^2} + \left(k_0^2 - \beta^2\right) E_y = 0, & \text{(2.18a)} \\
H_x = -\dfrac{\beta}{\omega\mu_0} E_y, & \text{(2.18b)} \\
H_z = \dfrac{i}{\omega\mu_0} \dfrac{\partial E_y}{\partial x}, & \text{(2.18c)}
\end{cases}
$$

and

$$
\text{(TM)} \begin{cases}
\dfrac{\partial}{\partial x}\left(\dfrac{1}{n^2}\dfrac{\partial H_y}{\partial x}\right) + \left(k_0^2 - \dfrac{\beta^2}{n^2}\right) H_y = 0, & \text{(2.19a)} \\
E_x = \dfrac{\beta}{\omega\varepsilon_0 n^2} H_y, & \text{(2.19b)} \\
E_z = -\dfrac{i}{\omega\varepsilon_0 n^2} \dfrac{\partial H_y}{\partial x}, & \text{(2.19c)}
\end{cases}
$$

where we have used $k_0^2 = \omega^2 \varepsilon_0 \mu_0$, with k_0 being the wavenumber in vacuum. Because the two sets of equations are linearly independent, all solutions to the Maxwell's equations (2.14) may be expressed as linear combinations of solutions to (2.18) with $E_x = E_z = H_y = 0$ and (2.19) with $H_x = H_z = E_y = 0$. Because the electric field is transverse to the direction of propagation in the former set of solutions, they are called the transverse electric, or TE modes. Solutions to the latter set of equations are called the transverse magnetic, or TM modes, since the magnetic field is transverse to the direction of propagation. Orientations of the electric and magnetic fields in the TE and TM modes of a dielectric slab waveguide are illustrated in Fig. 2.4.

2.2.2 Dispersion relations of the TE and TM modes

One may note that the only boundary conditions we have put into the Maxwell's equations thus far, is that the solutions are propagating (only) in the z-direction (along the slab). This way we have obtained the electromagnetic equations for the dielectric slab waveguide, and found that there are two linearly independent sets of equations, which depict the TE and TM modes. In order to obtain the dispersion relation for the TE mode, one must find the solutions to equation (2.18a), with appropriate boundary conditions, *i.e.* we require that the electric field decays exponentially in the cladding and the substrate. Furthermore, the tangential electric field must be continuous at the interfaces of the different media. The ansatz for electric field of the TE modes may thus be written as

$$E_y = \begin{cases} A\cos(-\kappa a - \phi)e^{\alpha_s(x+a)}e^{i(\beta z - \omega t)}, & x < -a, \\ A\cos(\kappa x - \phi)e^{i(\beta z - \omega t)}, & -a < x < a, \\ A\cos(\kappa a - \phi)e^{-\alpha_0(x-a)}e^{i(\beta z - \omega t)}, & x > a. \end{cases} \tag{2.20}$$

Here A is a constant amplitude, α_s, α_0 and κ are the x-wavenumbers at the substrate, cladding and core, respectively and β is again the propagation constant. Thickness of the core is $2a$ (see Fig. 2.3) and the phase factor is denoted with ϕ. Substituting each part of the ansatz (2.20), one at the time, into (2.18a) yields

$$\alpha_s = \sqrt{\beta^2 - k_0^2 n_s^2}, \tag{2.21a}$$

$$\kappa = \sqrt{k_0^2 n_1^2 - \beta^2}, \tag{2.21b}$$

$$\alpha_0 = \sqrt{\beta^2 - k_0^2 n_0^2}. \tag{2.21c}$$

From equations (2.21) one may find that the wave numbers κ, α_0 and α_s depend on each other in the following manner:

$$\kappa^2 + \alpha_s^2 = k_0^2(n_1^2 - n_s^2) \equiv \nu^2, \tag{2.22a}$$

$$\alpha_0 = \sqrt{\gamma\nu^2 + \alpha_s^2}, \tag{2.22b}$$

$$\gamma \equiv \frac{n_s^2 - n_0^2}{n_1^2 - n_s^2}. \tag{2.22c}$$

Other boundary condition one may use is that the tangential component of magnetic field, H_z, must be continuous at the interfaces. Substituting each part of the ansatz (2.20) into the expression for H_z in TE modes (2.18c), and requiring continuity of H_z at $x = -a$ and $x = a$ eventually leads to dispersion relations for the TE modes:

$$
(\mathrm{TE})\begin{cases} \kappa = \dfrac{1}{2a}\left(\arctan\left(\dfrac{\alpha_s}{\kappa}\right) + \arctan\left(\dfrac{\alpha_0}{\kappa}\right) + m\pi\right), & (2.23\mathrm{a}) \\ \phi = \dfrac{1}{2a}\left(\arctan\left(\dfrac{\alpha_s}{\kappa}\right) - \arctan\left(\dfrac{\alpha_0}{\kappa}\right) + m\pi\right), & (2.23\mathrm{b}) \end{cases}
$$

where m is a non-negative integer. TE modes corresponding to solutions of (2.23) with different m are labeled TE_0, TE_1, TE_2 and so forth.

In similar fashion, dispersion relations for the TM modes may be found. By substituting trial functions for H_y,

$$
H_y = \begin{cases} A\cos(-\kappa a - \phi)e^{\alpha_s(x+a)}e^{i(\beta z - \omega t)}, & x < -a, \\ A\cos(\kappa x - \phi)e^{i(\beta z - \omega t)}, & -a < x < a, \\ A\cos(\kappa a - \phi)e^{-\alpha_0(x-a)}e^{i(\beta z - \omega t)}, & x > a, \end{cases} \tag{2.24}
$$

into the electromagnetic equation for TM-modes (2.19) one obtains equations (2.21) and (2.22) once again. By using the continuity of E_z at the boundaries, following dispersion relations for the TM-modes are obtained:

$$
(\mathrm{TM})\begin{cases} \kappa = \dfrac{1}{2a}\left(\arctan\left(\dfrac{\alpha_s n_1^2}{\kappa n_s^2}\right) + \arctan\left(\dfrac{\alpha_0 n_1^2}{\kappa n_0^2}\right) + m\pi\right), & (2.25\mathrm{a}) \\ \phi = \dfrac{1}{2a}\left(\arctan\left(\dfrac{\alpha_s n_1^2}{\kappa n_s^2}\right) - \arctan\left(\dfrac{\alpha_0 n_1^2}{\kappa n_0^2}\right) + m\pi\right). & (2.25\mathrm{b}) \end{cases}
$$

2.2.3 Field profiles

Field profiles for the TE and TM fields are presented in equations (2.20) and (2.24). In order to plot the fields one must find out the values for the x-wavenumbers α_s, α_0 and κ. In general case there are no analytical expressions for these, but equations (2.23), (2.25) and (2.22) may be used to find them numerically. Core thickness a and refractive indices n_s, n_1 and n_0 are defined by the waveguide, and for a given vacuum wavelength, parameter ν is fixed by (2.22a). Iterative process then has to be used to find the wavenumbers: (i) As first step, one sets a trial value for one of the wavenumbers α_s, α_0 or κ and uses equations (2.22) to obtain values for the remaining ones. (ii) Next, these are substituted into equation (2.23) (TE-modes) or (2.25) (TM-modes), with a given mode m. If the obtained wavenumbers do not fulfill the equation, a new trial value for the initial wavenumber is selected, and steps (i) and (ii) are repeated until wavenumbers fulfilling the dispersion relation are found. In Fig. 2.5 field profiles, obtained in aforementioned manner by using a MATLAB® code, for

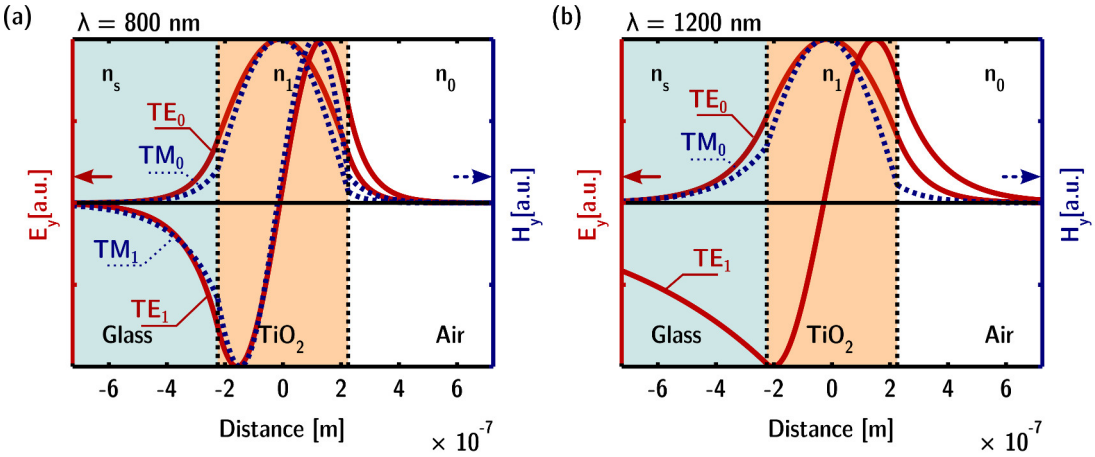

Figure 2.5: Electric/magnetic field profiles for TE/TM modes in a dielectric slab waveguide for vacuum wavelength of (a) 800 nm and (b) 1200 nm. Parameters used in calculation: core thickness $d = 450$ nm; $n_s = 1.51$ (soda-lime glass); $n_0 = 1$ (air); $n_1 = 2.345$ (TiO_2) in (a) and 2.306 in (b). Refractive indices for TiO_2 are taken from measurements.

TE and TM modes supported by a 450 nm thick TiO_2 layer on soda-lime glass substrate in air are presented for vacuum wavelengths of 800 and 1200 nm.

For a given wavelength, a slab waveguide may support several modes. The thinner the waveguide, the less modes it can support for a given wavelength. Furthermore, there is a cut-off wavelength for a given mode; for that particular mode wavelengths longer than the cut-off wavelength are not allowed. For thinner waveguide the cut-off wavelength for a given mode is shorter. As the wavelength increases or the waveguide thickness decreases, the higher order modes are cut-off first. Decreasing the refractive index contrast between the core and substrate or core and cladding shortens the cut-off wavelength for a given mode, and a waveguide with smaller refractive index contrast supports less modes for a given wavelength.

In Fig. 2.5 one may notice that the 450 nm glass/TiO_2/air waveguide supports two TE and two TM modes at 800 nm and that the TM_1 mode is cut-off when wavelength is increased to 1200 nm. The exponentially decaying tail of the TE_1 mode extends much further into the glass substrate at $\lambda = 1200$ nm, as the mode approaches cut-off. It is said that near cut-off the confinement of the mode gets weaker, and larger fraction of the energy of the mode is propagated outside of the core.

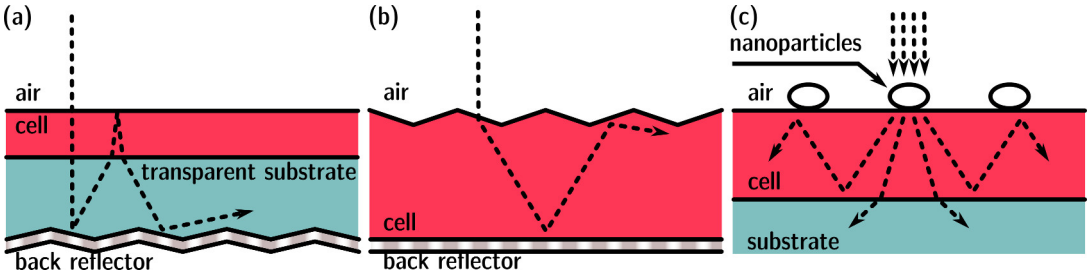

Figure 2.6: Geometrical light trapping schemes in thin-film Si solar cells using (a) an angled back reflector and (b) surface texturing with a flat back reflector. (c) Light trapping using plasmonic nanoparticles to scatter light into guided modes of the silicon film.

2.3 Plasmon enhanced thin-film solar cells

Main benefits of thin-film solar cells, compared to the 1st generation wafer based silicon cells, include reduced manufacturing costs, achieved via reduced amount of semiconductor material needed; loosened requirements for material quality (because shorter carrier diffusion lenght is needed); large scale manufacturability on cheap substrates and the increased open-circuit voltage via decreased bulk charge recombination [14] [15, pp.27–35]. These benefits don't come without drawbacks though, and the efficiencies of thin-film solar modules are still up to 50 % lower than those of wafer based Si modules, owing to poor absorption during single passing of light through the thin semiconductor layer [15, pp.27–35].

Light absorption in thin solar cells may be improved by increasing the optical path length of light through the device. This is known as light-trapping. Enhancing the efficiency of thin-film solar cells via multiple passing of light was proposed as early as 1974 by Redfield [14], by using angled back reflector (see Fig. 2.6(a)): light at the normal incidence is reflected from the back reflector in an angle such that the ray exhibits a total internal reflection at the front surface, and is returned to the cell. In 1987 Campbell and Green examined light trapping via pyramidal microtexturing of the silicon surface, as illustrated in two dimensions in Fig. 2.6(b)) [16]: here the light entering the cell is refracted at an angle by the textured front surface and may be trapped inside the cell via reflection from the back reflector and total internal reflection at the front surface. In addition to the aforementioned geometrical light-trapping schemes a so-called Lambertian light-trapping may be utilized, where the surface roughness of the semiconductor and/or the back reflector is optimized so that random Lambertian scattering occurs [17, 18].

While the texturing of the semiconductor surfaces provides an efficient means for light trapping, it also limits the minimum thickness of the cell and increases the surface recombination via increased surface area. Thus, in thin solar cells with thickness in the order of few hundred nanometers, an alternative solution for the light trapping becomes necessary.[1] One proposed method to achieve optical path length enhancement without tampering with the silicon surface is by plasmonic nanoparticles. Using plasmonic nanoparticles for the light trapping in solar cells was first proposed in 1996 by Stuart and Hall, who observed an enhancement in the optical absorption in silicon-on-insulator (SOI) waveguides by plasmonic metal island films, deposited on the device surface [19]. Here, and in their following works [20, 21], enhancements up to factor 20 in photocurrent generation at near infra-red (NIR) wavelengths in SOI photodiodes were presented. These results were attributed to waveguide-mediated dipole-dipole interactions between the plasmonic particles [19]. Furthermore, based on the measured scattering spectra and theoretically calculated coupling ranges for the waveguide modes, Stuart and Hall showed that the plasmon-waveguide coupling is determined by the modal structure of the waveguide [20]. In the following years, Soller and Hall showed by theoretical calculations that the enhancements were indeed due to individual particles acting as nanoscale, horizontal dipole antennas, coupling light into the guided modes [22, 23], and that the scattering properties of the particles were significantly modified by the waveguide mediated dipole-dipole interactions [24].

After a long silence in the field of plasmon enhanced solar cells, in 2006, Derkacs *et al.* demonstrated improved performance of an amorphous silicon thin-film solar cell via scattering of light by plasmonic nanoparticles [25]. They attributed the increased current and power output of the measured a-Si cells to consentration of electric fields in the semiconductor due to forward scattering by the metal nanoparticles. Unlike Stuart and Hall they did not consider the waveguide effects of the thin silicon layer in their discussion. Absorption enhancements on SOI based devices by plasmonic particles were again brought under investigation by Catchpole and Pillai *et al.* in 2006–7 [26–29]. 2007 Pillai *et al.* demonstrated photocurrent enhancement on both a SOI-based thin-film silicon test cell and a thick wafer based Si solar cell [29].

In the light of current knowledge the light-trapping via plasmonic particles is based on the high scattering efficiency of the localized surface plasmons into high refractive index substrate; when a dipole is located near an interface between

[1] During recent years nanotexturing of silicon surfaces has become feasible, allowing for substantial increases in absorptance even in very thin silicon films. However, the increased surface recombination still remains a problem.

two media, the scattering is directed preferentially into the medium with higher refractive index [30]. The angular spread of the scattered light increases the optical path length, and some fraction of the light scattered into the substrate may be trapped within the cell as a waveguide mode [6], provided that conditions for conservation of energy and momentum are satisfied (see Fig. 2.6(c)).

The most notable problems in the plasmon enhanced solar cells (and most often presented arguments against them) are the destructive interference of the electric field scattered by the particle and the incident field [31–35], and the absorption of the incident light by the nanoparticles [36]. Both of these may be avoided simply by placing the particles on the rear side of the cell. With rear located particles, only that fraction of light which is initially not absorbed within the cell is affected by the particles [28,36] and the destructive interference of fields in the forward direction (in respect to the incident radiation) does not affect the carrier generation in the cell [33, 34, 36–38]. Despite the promising results in numerous publications, a functional plasmonic solar cell demonstrating overall performance enhancement over conventional, non-plasmonic ones is still yet to be reported.

2.4 Window glass integrated solar concentrator

The consept of solar concentrators based on waveguiding effect is not a new one. Already in 1977, Goetzberger & Greubel proposed a method for solar energy conversion, using fluorescent molecules embedded in transparent sheets; the dyes would absorb and re-emit light into the transparent sheet, which would then act as a waveguide and concentrate the re-emitted light into photovoltaic cells [39]. This would (i) present an economically feasible means to collect light from larger surface areas and consentrate it into smaller surface of expensive, high quality solar cells, and (ii) by using different dyes in separate layers of the collector, allow separation of solar spectrum into different bands and to direct the different bands of solar radiation into solar cells with different, optimized band-gaps [39]. This luminescent solar concentrator (LSC) concept and its potential in solar energy conversion has since been thoroughly investigated [40, 41], and one of the most recent advances in LSC research, named the organic solar consentrator (OSC), was reported by Currie *et al.* in *Science* 2008 [42].

However, the utilization of the principles of LSC/OSC in window integrated solar energy conversion has not been considered previously. When using dye molecules one would have to limit the solar energy collection to ultraviolet spec-

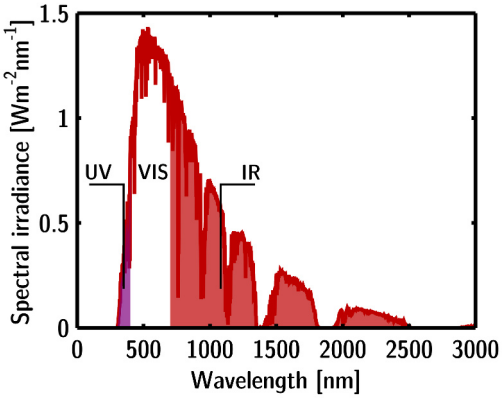

Figure 2.7: The air mass (AM) 1.5 solar spectrum, direct plus diffuse circumsolar irradiance. Ultraviolet, visible and infrared portions of the solar spectrum are indicated. Data from ASTM G173-03 reference spectrum [43].

tral range or compromise the transparency of the window glass on visible wavelengths. The former severely limits the amount of spectral energy available for conversion, and the latter the usability of the integrated collector as a window. Plasmonic nanoparticles would enable the collection and trapping of light at near-infrared wavelengths, which constitutes a large fraction of the total solar irradiation (see Fig. 2.7).

3

Experimental

Initially, to prove the proposed window integrated solar concentrator concept, measurements were set up, in which absorber paint coated copper tubes were installed around titanium dioxide (TiO_2) coated $10 \times 10\,cm^2$, 1 mm thick glass pane covered with colloidal gold nanoparticles. Glass was illuminated with a broadband light source and the temperature of water circulated in the tubes was measured over a period of several hours at the inlet and the outlet. However, no substantial heating of the circulating water could be detected. In order to explain the results of the water circulation experiment, optical measurements on light coupling into a planar waveguide by plasmonic nanoparticles and the propagation of light within the waveguide were planned. To this end, samples with nanoparticles either on a plain 1 mm thick soda-lime glass slide or on a glass slide with a separate high-refractive-index waveguide layer were fabricated. The basic measurement geometry is illustrated in Fig. 3.1: The sample is illuminated

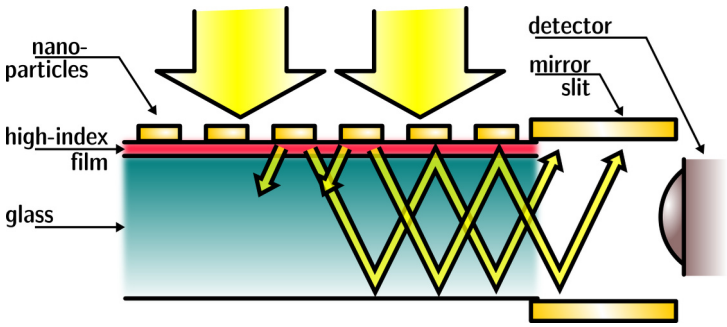

Figure 3.1: Illustration of a sample and the optical measurement geometry used in the emission measurements.

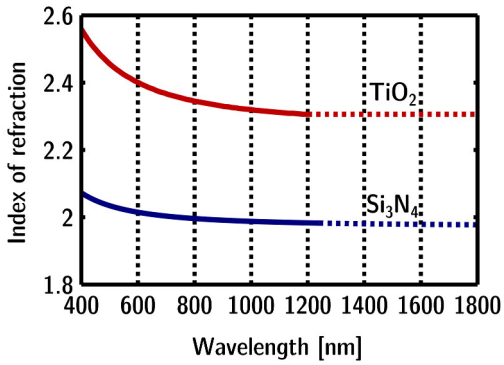

Figure 3.2: Refractive index n of TiO_2 (data from Beneq) and Si_3N_4 (expression from Bååk [44]. Dotted lines denote extrapolated data.

with normal incidence and some part of the incident light is scattered by the plasmonic particles into the substrate and coupled into the waveguide. The light emitted out of the waveguide edge is then measured by a photodiode at the side of the sample. Also, different nanoparticle geometries and fabrication methods were considered.

3.1 Sample fabrication and characterization

Silicon nitride (Si_3N_4) and (TiO_2) were selected as materials for the high refractive index waveguides. TiO_2 has the higher refractive index of the two materials (see Fig. 3.2), but Si_3N_4 thin films could be deposited with the plasma enhanced chemical vapour deposition (PECVD) machine in our own clean room facilities. TiO_2 films were grown by atomic layer deposition (ALD) by Beneq.

Gold was selected as the nanoparticle material because it has plasmon resonance at longer wavelength and is more resistant to oxidation than other metals often used in plasmonics, such as silver and aluminum. Initially, coating with commercially available colloidal gold nanospheres of 150 nm diameter (from British Biocell International) was utilized to obtain coverage of plasmonic nanoparticles on the samples. However, it soon became apparent that the particle coverage achieved with this method was not uniform or high enough for sufficient scattering effect (see Fig. 3.3). After that, two other particle fabrication methods, metal island film evaporation and hole-mask colloidal lithography (HCL) [45], were investigated.

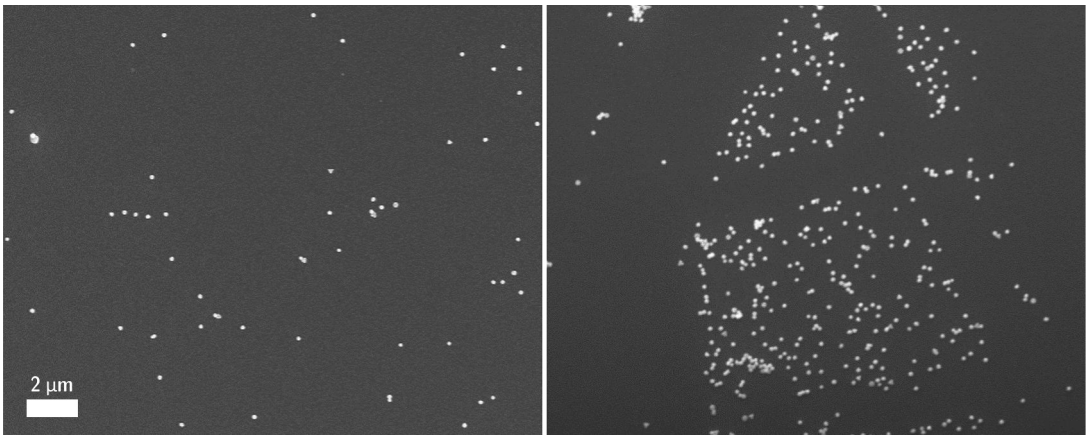

Figure 3.3: SEM images of 150 nm diameter spherical colloidal gold nanoparticles on a glass slide.

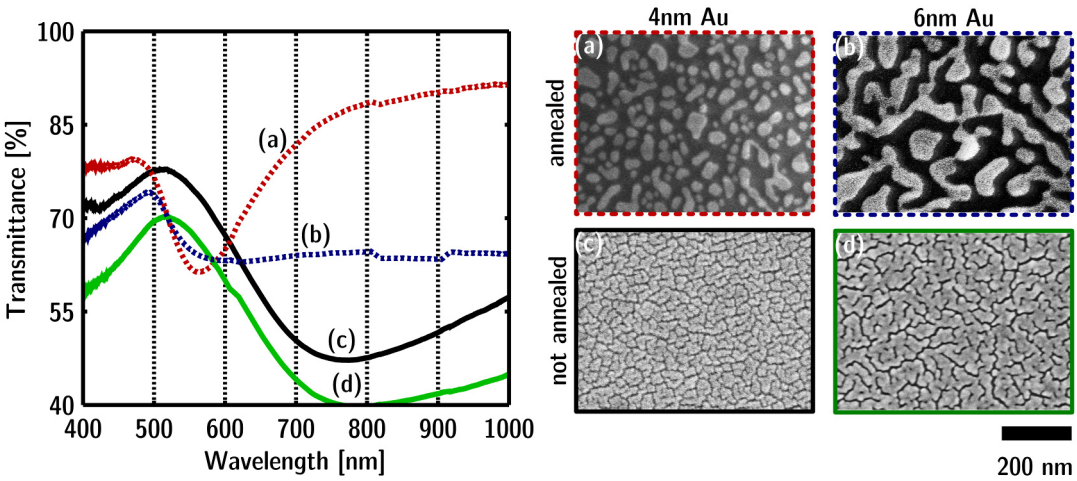

Figure 3.4: Effect of annealing on Au island film formation. Big image: Transmittance spectra of the annealed and unannealed 4 and 6 nm thick Au island films on glass. Insets (a)–(d): SEM images of the island films.

3.1.1 Metal island film evaporation

Fabrication of metal island films, similar to those used in refs. [19–21, 26–29], by electron beam evaporation was experimented with varying process parameters. Metal island formation occurs when the deposited thickness is too small to produce a continuous metal film. Varied fabrication parameters included deposited material thickness, deposition rate and annealing temperature, together with heating of the sample during the deposition.

On unheated glass substrates it was observed that Au film thickness around 4 – 5 nm would produce a porous film, but not distinct metal islands. Annealing of the samples after the Au film deposition, in temperatures ranging from 250 °C to 350 °C for duration of 50 minutes, increased the porosity in thicker films (6–8 nm) and resulted in formation of discrete metal islands in case of smaller film thicknesses (4–6 nm), via surface tension (see insets of Fig. 3.4). Transmittance spectra (big image on Fig. 3.4) show distinct differences between the annealed and unannealed films; the unannealed films show a broad resonance (transmittance minima) just under 800 nm, whereas the annealed sample with 4 nm Au thickness has narrower plasmonic resonance around 560 nm. The annealed 6 nm Au film shows a broad plasmonic feature extending from 560 nm to the end of the measurement range at 1000 nm, which results from the elongated shape of the features of the gold film (ellipsoidal particles also show this kind of extended resonance under unpolarized illumination).

Substrate heating during the film deposition was employed to achieve metal island formation on higher film thicknesse, and greater average island diameter. The result was that the maximum Au film thickness for distinct metal island formation increased from around 4 to 5 nm, with the substrate heating, but island size did not change significantly. Finally, Si_3N_4 overcoatings of different thickness were utilized to tune the plasmon resonance wavelength. It is well known that the LSPR wavelength may be shifted by chanching the dielectric environment of the plasmonic particles [46], but the effect of the dielectric coating thickness on the resonance shift has not been studied systematically. Here, the thickness of Si_3N_4 overcoating was varied from 5 to 180 nm. Results are shown in Fig. 3.5. At first, the LSPR wavelength increases rapidly as the Si_3N_4 thickness increases, but after 50 nm coating thickness the resonance is not shifted further. This is in agreement with the fact that the near field of the plasmon decays exponentially in distance from the particle surface; thus the effect of the dielectric overcoating is strongest at the first few nanometers of the coating thickness, but as the distance from the particle increases, the particle does not sense the presence of additional overcoating so strongly anymore.

In conclusion, while precise control over particle size or shape cannot be achieved by the metal island evaporation, it is possible to coarsely tune the plasmonic resonance wavelength. Also, the resonance may be red-shifted in a controllable way by overcoating the particles with a high refractive index material.

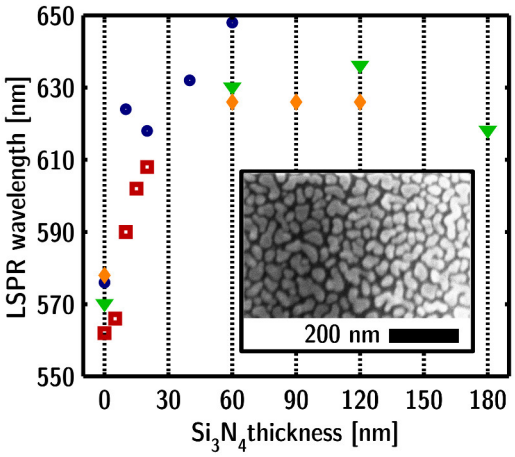

Figure 3.5: Effect of a dielectric overcoating on the LSPR wavelength of a 5 nm thick Au island film on glass. Samples made in same Au film deposition run are marked with same symbol. Inset: SEM image of a bare 5 nm Au island film on glass.

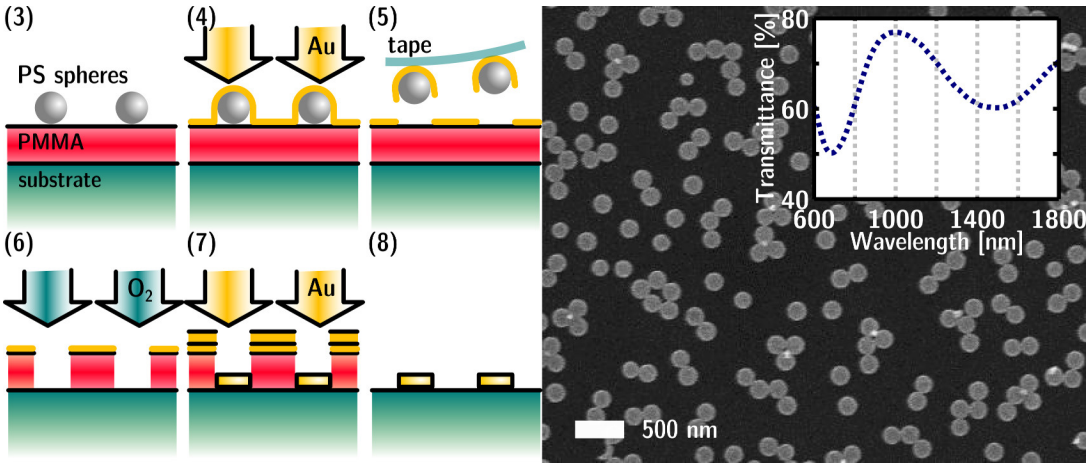

Figure 3.6: Left: The hole-mask colloidal lithography (HCL) process. Right: SEM image of Au nanodisks made by HCL. Inset: Transmittance spectrum of the Au nanodisks on glass.

3.1.2 Hole-mask colloidal lithography

The final candidate for the method of nanoparticle fabrication for the measurements of the waveguide coupling was the hole-mask colloidal lithography (HCL) [45]. The process, as used in the fabrication of the samples for the measurements presented in this thesis work, typically proceeded as follows (see subfigures (3–8) of Fig.3.6):

(1) A sacrificial layer of Poly(methyl methacrylate) (MicroChem 495 PMMA, 2 wt% in anisole) was spin coated on the substrate, in this case either a plain glass slide or a glass slide overcoated with a dielectric film, at 2000 rpm for 1 minute, and the sample was baked for 10 minutes in order to remove solvent and to anneal the PMMA film.

(2) The sample was treated with O_2 plasma by reactive ion etching machine (RIE), with low power and for short duration (50 W, 5 seconds) in order to make the PMMA film hydrophilic.

(3) The sample was covered with Poly(diallyldimethylammonium chloride) (PDDA) solution (0.2 wt% in water) for duration of 30 s, by pipetting, then rinsed with de-ionized water for another 30 seconds and dried by pressing gently with a clean room sheet. Sample was then covered with solution of commercially available polystyrene-latex (PS) nanospheres (0.2 wt% in water) for duration of 2 min, then rinsed with DI water for 1 min and pressed dry with a clean room sheet. The size of the PS spheres determines the size of the holes in the hole-mask. The diameter of PS nanospheres used in this work was 200 nm. The PDDA polyelectrolyte functions as a positively charged screening medium for the negatively surface-charged PS spheres, to decrease the inter-particle repulsion. Samples were dried with clean room sheets instead of blowing with nitrogen gas to prevent the PDDA from flowing unevenly across the surface and the agglomeration of the PS spheres, in order to produce a homogenous distribution of nanoparticles across the whole sample area. The aforementioned concentrations of the PDDA and PS-particle solutions are optimized for the 200 nm diameter circular nanodisks. For greater inter-particle separation, the PDDA and PS-particle solutions may be diluted, and vice versa for smaller particle separation.

(4) Deposition of the hole-mask layer was then performed by electron beam evaporation in ultra high vacuum (UHV). In this work, gold layer was used as the mask and evaporated thickness was 14 nm. Evaporation angle normal to the surface was used to produce mask with circular holes. Ellipsoidal particles with desired semi-major to semi-minor axis ratio may be fabricated by using a different evaporation angle.

(5) After the mask evaporation PS spheres were lifted-off from the sample by pressing a transparent tape on the sample surface and then gently pulling

the tape off. The PS beads attach to the tape, but rest of the metal layer is left intact, thus forming the hole-mask.

(6) Holes were then etched to the PMMA through the hole-mask by oxygen plasma in RIE (50 W, 1.2 mins).

(7) Desired thickness of Au was deposited by electron beam evaporation in UHV to form the nanoparticles. Height of the nanoparticles is controlled by the deposited thickness, and limited essentially by the thickness of the sacrificial PMMA layer. The cross-section of the nanoparticles is determined by the size and shape of the holes in the hole-mask.

(8) Lift-off was performed by ultrasonicating the sample for 5 minutes in acetone heated to its boiling point, and rinsing with isopropanol and DI water. Finally the sample was blow-dried with nitrogen gas.

The hole-mask colloidal lithography method produces a sufficiently large particle density across a large surface area (a few square centimeters) and a highly narrow particle size distribution, determined by the size of PS spheres used for the hole-mask formation. This, together with the repeatibility of the particle density and size from sample to sample, was the main reason for the selection of HCL as the method to be used in the fabrication of the samples for the nanoparticle-waveguide coupling experiments.

3.2 Results and discussion

3.2.1 Emission measurements

The coupling of light into the guided modes by plasmonic particles was investigated by illuminating the sample from the front (particle coated side) or rear, and measuring the intensity of the light emitted out of the sample edge, as illustrated in Fig. 3.1. These measurements are henceforth referred to as emission (EMS) measurements in this thesis. A schematic illustration of the measurement setup is shown in Fig. 3.7. The light emission from the sample edge was measured with an encased AC-coupled amplified PbS photodiode (Thorlabs PDA-30G-EC). Because the photodiode does not resolve different wavelengths, a monochromator (Acton SP-2155 with 750 grooves/mm grating) was used to scan through the desired wavelength range of the incident illumination from an Oriel model 66182 light source. To exclude external light from the measurement, the intensity of the incident light was modulated with an optical fork chopper, located at the entrance slit of the monochromator, and the voltage output of the photodetector was fed to a lock-in amplifier, together with the reference signal from the chopper. Higher order reflections from the monochromator grating were eliminated

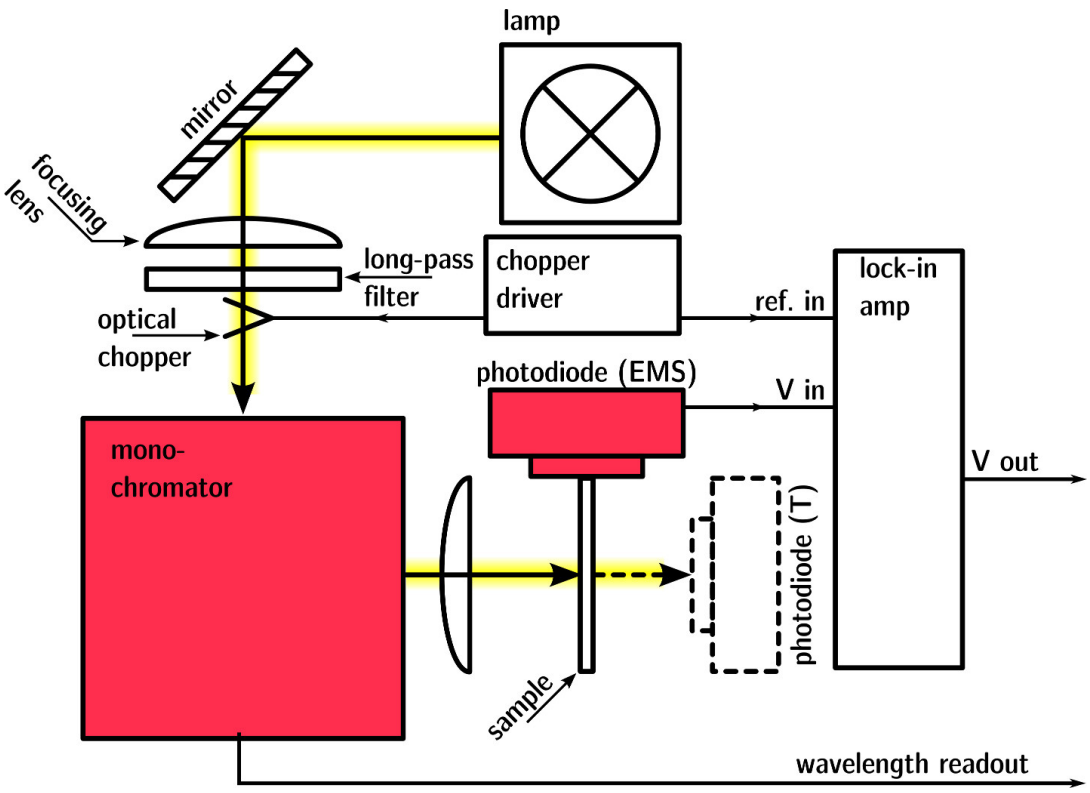

Figure 3.7: Schematic illustration of the emission (EMS) measurement setup. Transmittance was measured with detector at the position as indicated with (T).

with a long-pass filter (with a cut-off wavelength of 600 or 1200 nm, depending on the measurement range) situated at the entrance slit. In order to compensate the response of the photodiode to different wavelengths, illumination from the monochromator without a sample was measured as a reference, with which the emissions measured from the samples were then normalized. The same measurement setup was also used to measure transmittances of the samples, by first measuring the transmitted intensity through a plain glass slide, and then the transmitted intensity through the sample.

First emission measurements were performed on samples with silicon nitride waveguides and gold nanodisks. However, the PECVD Si_3N_4 thin films proved to be of low quality; transmittance spectra of the fabricated samples revealed absence of any thin-film interference patterns, which is an indicator of substantial inhomogenities in the thickness and/or optical quality of the film. Several mainteinances performed on the PECVD machine did not fix this problem, and thus a

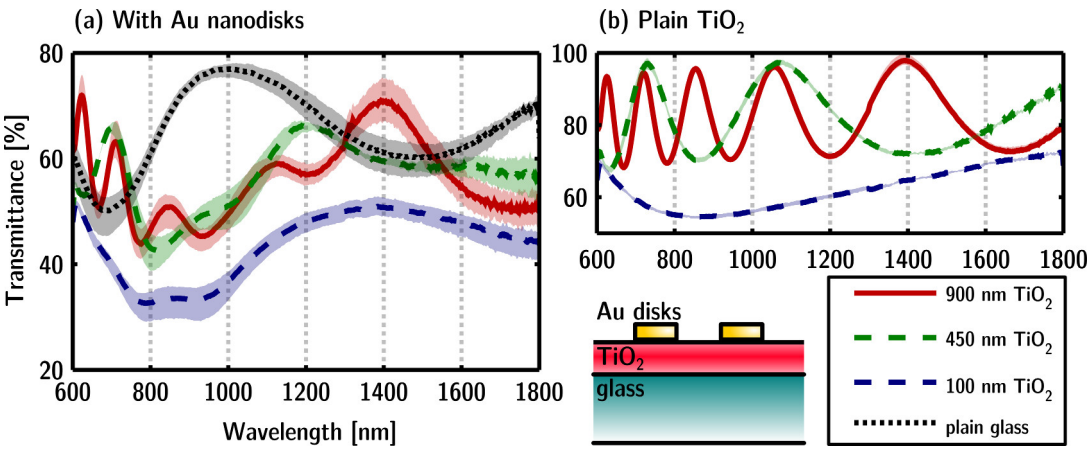

Figure 3.8: (a) Transmittances of TiO_2 films with circular 42×200 nm Au nanodisks (height × diameter). (b) Transmittances of the corresponding TiO_2 films without the nanoparticles. Colored bands around the lines show the maximum error limits.

decision was made to abandon the measurements with silicon nitride waveguides and to proceed with the ALD-made titanium dioxide films only. These experiments will be discussed here mostly to the extent that is relevant to the window integrated solar consentrator application, as they are presented in greater detail, and in broader context, within the included publication (Appendix A).

First of all, it was observed that the nanoparticles do scatter and couple light into the waveguide, and that the coupling is most efficient at the wavelengths corresponding to the plasmonic resonances on the particles. The wavelengths at which the plasmonic resonances of the particles occur may be discerned from the transmittance spectra of the samples, shown in Fig. 3.8(a). In case of particles on plain glass substrate (dotted black line) the local minima show the locations of the resonances. The titanium dioxide films make it more difficult to distinguish the local minima corresponding to the plasmonic resonances from the minima coused by the thin-film interferences, as shown in Fig. 3.8(b). On a plain glass substrate the 200 nm diameter and 42 nm high gold nanodisks have plasmonic resonance at around 700 nm and another one at around 1450 nm. These are red-shifted to around 850 nm and above 1800 nm (beyond the range of our measurements), respectively, by the TiO_2 films. Some computational studies [47] suggest that the two distinct plasmonic resonances arise from different electric field localizations; at the shorter-wavelength resonance the electric field is strongest at the interface between the particle and air, while in the longer-wavelength resonance the field is localized to the particle-substrate interface.

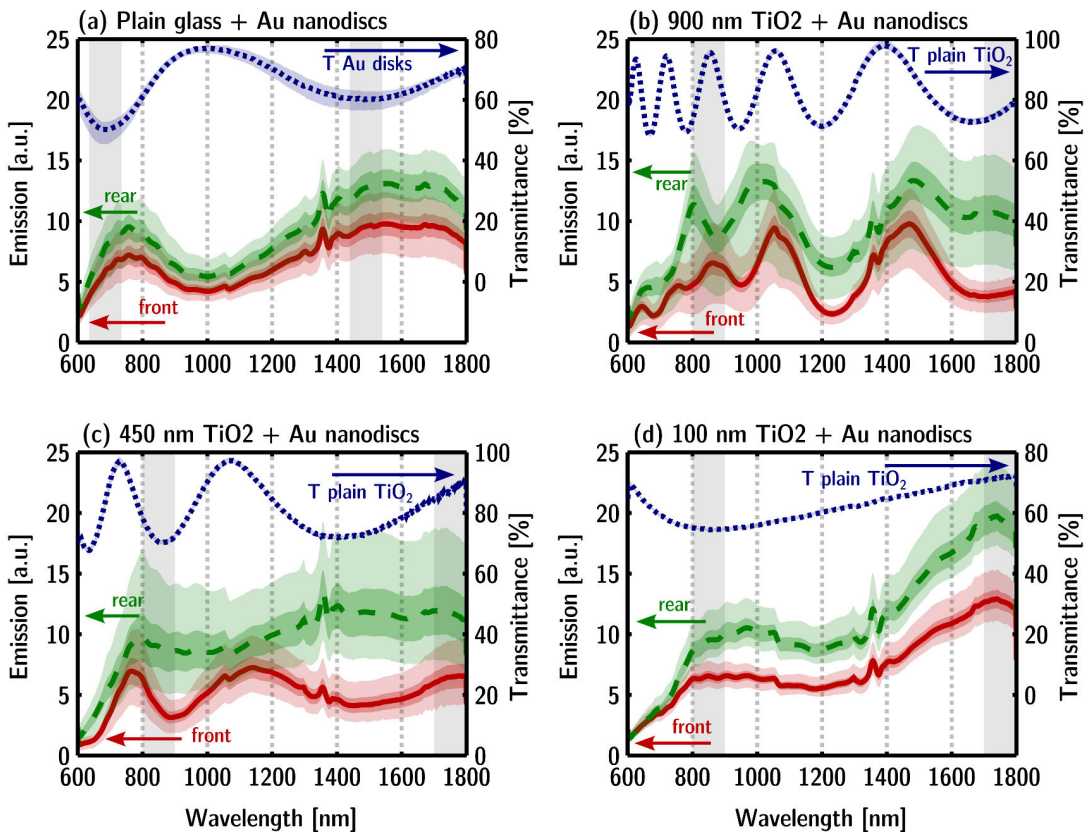

Figure 3.9: Results of emission measurements of the samples with circular 42×200 nm Au nanodisks (height × diameter) on (a) plain glass and on glass coated with (b) 900, (c) 450 and (d) 100 nm TiO_2 waveguides, with illumination of the sample from front (solid line) and rear (dashed line). Transmittance spectrum (dotted line) of the Au disks is shown for reference in (a) and transmittances of bare TiO_2 in (b–d), to illustrate the correspondence between the thin-film interference and the coupling efficiency. Vertical bands show locations of the LSP resonances.Colored bands around the lines show the 95 % confidence limits (inner bands) and maximum error limits (outer bands).

Another possible explanation is that the longer-wavelength feature arises from a collective resonance of two or more particles.

The scattering and coupling of light into the waveguide is illustrated by the emission measurements, shown in Fig. 3.9. The relation of the plasmonic resonances to the waveguide coupling is most evident in Fig. 3.9(a), where both the emission intensity and transmittance of the samples with Au nanodisks on plain glass slide are shown.

The emission measurements also showed that the glass itself acts as a waveguide as efficiently as the high-index TiO_2 film; this becomes evident by comparing the emission intensities in Figs. 3.9(a) (particles on bare glass) and (b–d) (particles on TiO_2 coated glass). The glass slide itself functions as a dielectric slab waveguide for the light scattered by the particles, as the refractive index of soda-lime glass $n \approx 1.5$ is higher than that of air $n \approx 1$. When the particles are deposited on a glass substrate coated with a thin-film with index of refraction higher than that of glass (and air), waveguiding occurs in both the high-index thin-film and glass. Although the refractive index of TiO_2 is considerably higher than that of glass, the thickness of the thin-films was three orders of magnitude smaller than thickness of the glass substrate, meaning that the number of modes supported by the high-index coating is much less than the number of modes supported by the glass substrate, for a given wavelength. Also, the cut-off wavelength of the combined high-index-film/glass-substrate waveguide is determined by the substrate thickness. In short; the wavelengths that do not "fit" into the high-index film may still be trapped because of the thick glass substrate.

From Figs. 3.9(a–d) it can be seen that although the addition of the high-refractive-index waveguide layer (TiO_2) causes an increase in the emission intensity, the increase is not very dramatic. The increase is most likely caused by the higher refractive index of TiO_2, compared to that of glass; it is known that plasmonic nanoparticles have higher scattering efficiency on higher refractive index substrate, and that on an interface their scattering is directed preferantially towards the higher index of refraction [48]. What is remarkable, however, is the effect of the thin-film interference to the emission; from Figs. 3.9(b–d) it is evident that under front illumination the local maxima of the emission spectra coincide with the interference maxima in transmittance. Under rear illumination there is also apparent interference effect in the emission spectra, but the peaks do not coincide with the interference peaks in transmittance. It is also of sifnificance that the emission intensity is always higher when the sample is illuminated from the rear, compared to the front illumination. This is most probably due to the effect of the interference to the electric field that is felt by

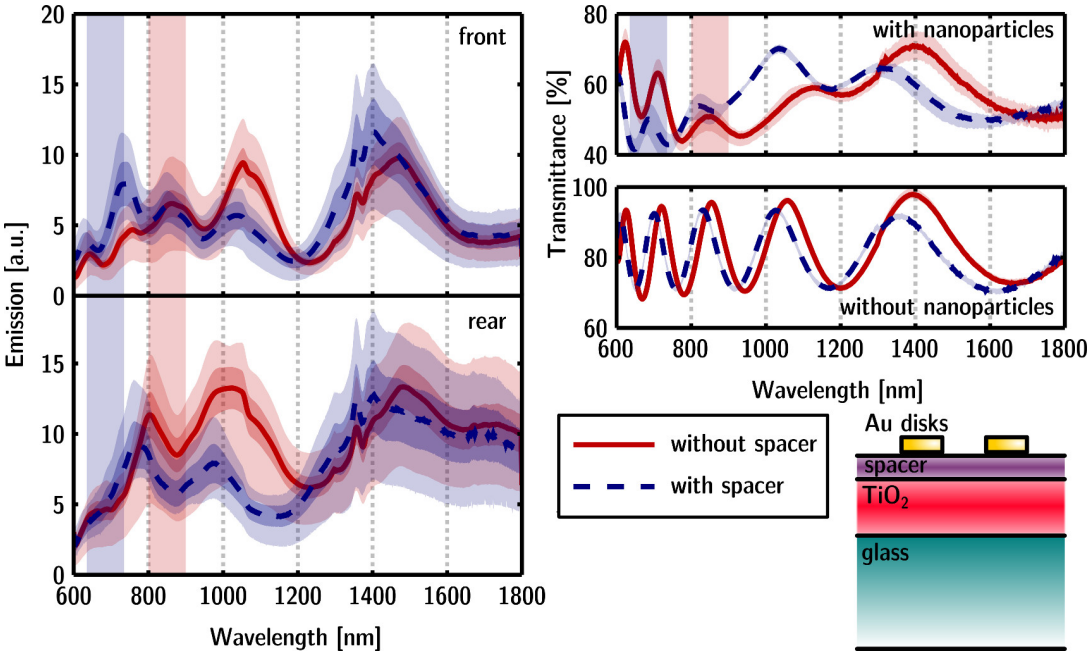

Figure 3.10: Effect of 50 nm aluminum oxide (ALO) spacer layer on the emission intensity (left) and transmittance (top right) of a sample with 900 nm TiO_2 film. Vertical bands show locations of the LSP resonances, obtained from the transmittance of the samples with the nanoparticles. Colored bands around the lines show the 95 % confidence limits (inner bands) and maximum error limits (outer bands). Inset in lower right corner shows the sample geometry.

the particles and causing the excitation of plasmons. This is discussed in more detail in the following section.

The effect of an additional layer of spacer material between the plasmonic particles and the titanium dioxide waveguide layer to the emission and waveguide coupling was also investigated (see inset of Fig. 3.10). Aluminum oxide (Al_2O_3) was used as the spacer material, having a refractive index of approximately 1.6, that is, considerably lower than that of TiO_2. The spacer layer alters the overlap of near electric field of the particles with the TiO_2, and this could be one design parameter in the window integrated solar consentrator for optimizing the plasmon-waveguide coupling. The most evident effect of the spacer layer is to shift the plasmonic resonance of the particles to shorter wavelength, due to lower refractive index of Al_2O_3, compared to that of TiO_2. There is no dramatic net effect on the overall emission by the addition of the spacer layer. However, in case of rear illumination, there is a small but noticeable decrease.

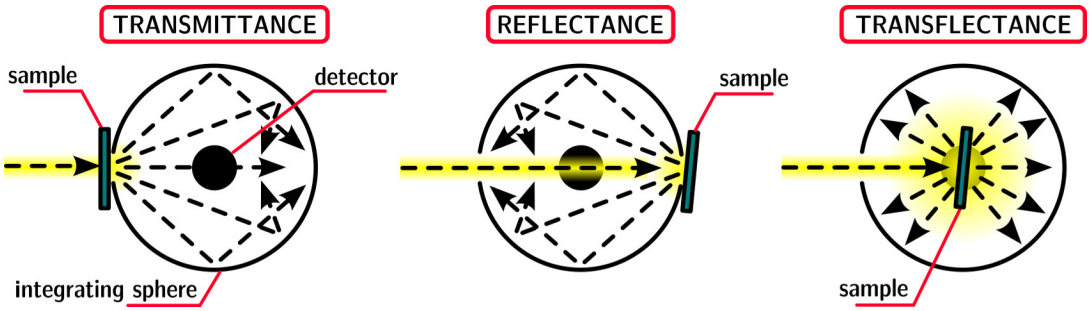

Figure 3.11: Measurement of total (beam plus diffuse) transmittance, total reflectance and total transflectance of a sample with an integrating sphere.

This is in agreement with some previous studies regarding plasmon enhanced solar cells [34, 36, 38].

However, the most crucial observation from the emission measurements, concerning the window integrated solar concentrator, is that the emission of light from the waveguide edge has very low intensity; it could be estimated that merely 0.1 % of incoming light was transmitted to and emitted from the waveguide edge. Furthermore, this is the efficiency of the $2.5 \times 2.5\,\mathrm{cm}^2$ samples made for the emission experiments; a device of a more practical size might have even poorer efficiency. This point is investigated more thoroughly in the following section of this thesis.

3.2.2 Integrating sphere measurements

In order to ascertain the results of emission measurements and to investigate the cause of poor emission intensity from the waveguide, one sample with 900 nm TiO_2 and circular 42 nm high Au nanodisks was selected for measurements with an integrating sphere and a spectrophotometer. The total absorptance of the sample was measured in two ways: (i) Separate measurement of total (beam plus diffuse) transmittance and total reflectance, where absorptance is obtained from

$$(\mathrm{Abs.}) = 100\,\% - (\mathrm{Trans.}) - (\mathrm{Refl.}), \tag{3.1}$$

and (ii) simultaneous measurement of both total transmittance and total reflectance, *i.e.* transflectance, where

$$(\mathrm{Abs.}) = 100\,\% - (\mathrm{Transfl.}). \tag{3.2}$$

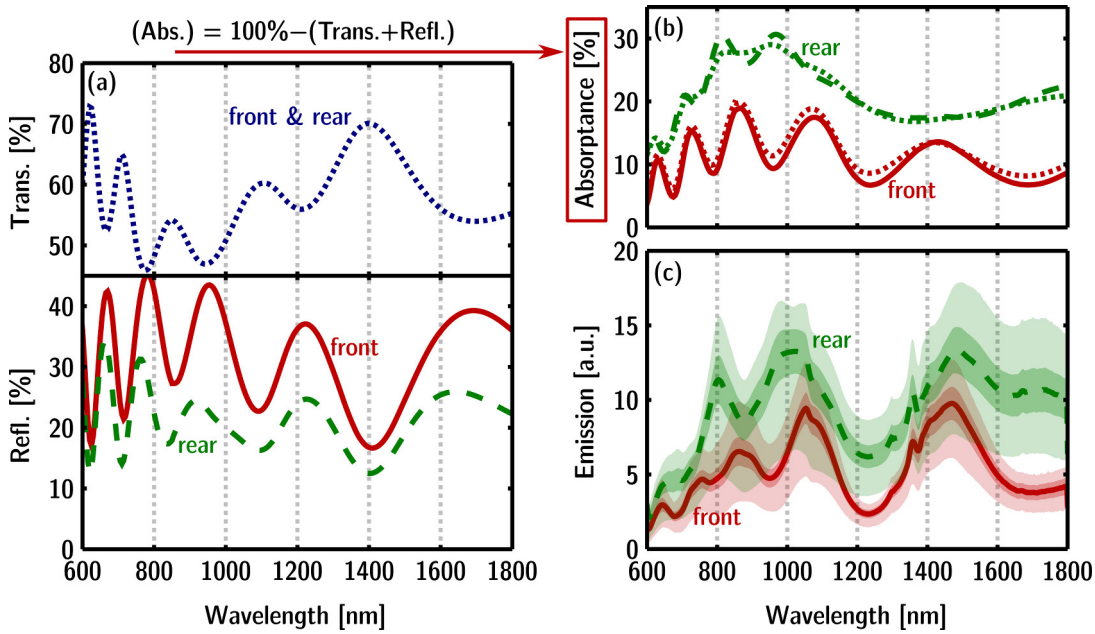

Figure 3.12: (a) Upper part: Total (beam plus diffuse) transmittance of a sample with 42 × 200 nm circular Au nanodisks and 900 nm TiO_2 on glass. Lower part: Total reflectance of the same sample, with illumination from front and rear. (b) Absorptance calculated from reflectance and transmittance, front and rear illumination (solid and dashed line). Absorptance from transflectance measurement, front and rear illumination (dotted lines). (c) Emission spectra, front and rear illumination, for the same sample, for comparison.

The difference between these two methods, as illustrated in Fig. 3.11, is that in the transflectance measurement (ii), the whole sample is placed within the integrating sphere; this means that light emitted out of the waveguide edge will also be collected by the sphere, whereas in the case of separate transmittance/reflectance measurements (i), the light emitted out of the waveguide will not be detected. Thus, the difference between the absorptance from the separate transmittance/reflectance measurements and the transflectance measurement equals the emission out of the sample edge.

The results of transmittance and reflectance measurements are shown in Fig. 3.12(a). The absorptances obtained by methods (i) and (ii) are presented in Fig. 3.12(b), showing that the difference between the absorptances by different methods is negligible. In other words, the emission from the waveguide edge is indeed as weak as observed in the direct emission measurements. What is interesting, however, is that the absorptance spectra of Fig. 3.12(b) have striking

similarity in shape to the emission spectra in Fig. 3.12(c), under both front and rear illumination. Furthermore, the absorption is also greater with rear illumination, as is the case also in the emission measurements.

From this we make two conclusions: (i) Since the interference shown in the reflectance and transmittance is also clearly visible in the emission spectra of front and rear illumination, the difference in coupling efficiency between different illumination directions is most probably caused by the interference in the electric field that excites the particle plasmons. (ii) Given the similarity of the absorptance and emission spectra, the plasmonic particles that are responsible for coupling the radiation into the waveguide also seem to cause the absorption of those very same guided modes. Even though the absorptance of the gold nanodisk monolayer is very small, the radiation propagating within the waveguide would interact with thousands of particles per millimeter along the path of propagation, thus causing exponential accumulation of the absorption effect. This presents a fundamental design problem for the proposed window integrated solar consentrator.

3.2.3 Emission measurements on ellipsoidal nanoparticles

We also investigated the effect of the polarization direction of linearly polarized incident light to the coupling efficiency of ellipsoidal nanoparticles. Samples with ellipsoidal Au nanodisks were illuminated with linearly polarized light at a normal incidence angle, and the intensity of light emitted out of the waveguide edge was measured, as described before in Chapter 3.2.1. The direction of the polarization was varied from 0° (polarization in the direction of the semi-major particle axis) to 90° (polarization in the direction of the semi-minor axis, see inset of Fig. 3.13).

Ellipsoidal Au nanoparticles with 200 and 400 nm semi-minor and semi-major axes, respectively, and 42 nm height were fabricated on 1 mm thick $2.5\times2.5\,\mathrm{cm}^2$ glass slides. Ellipsoidal particle shape was achieved by using a 60° evaporation angle (with respect to surface normal) in the mask evaporation step (4) of the HCL process (see Chapter 3.1.2). The PDDA electrolyte solution was diluted down to 0.005 wt% and PS-particle solution to 0.02 wt% in H_2O in order to increase inter-particle separation and prevent overlap of the particles of elongated, ellipsoidal shape.

A prism polarizer on a rotating mount was added to the exit of the monochromator, between the focusing lens and the sample in the direct optical measurement setup (see Fig. 3.7), to measure the transmittance and the emission out

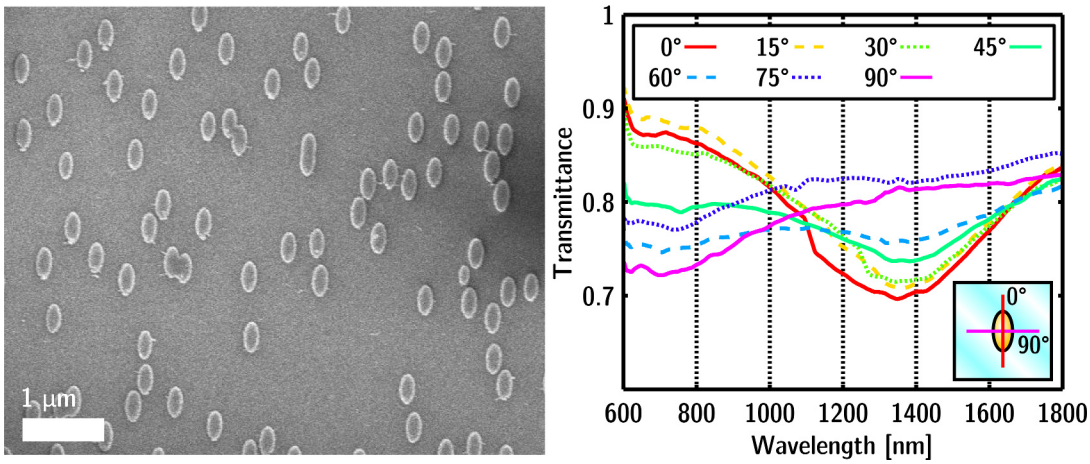

Figure 3.13: Left: A SEM image of ellipsoidal Au nanodisks on a glass substrate. Right: Transmittance of the ellipsoidal Au disks under illumination by linearly polarized light with different polarization directions. Inset shows the orientations of 0° and 90° polarization directions with respect to the particle orientation.

of the sample edge for different directions of polarization of the incident light. The optical fork chopper used in previous emission measurements to modulate the intensity of the light beam was substituted with a six-blade rotating optical chopper. Emission measurements were performed from all four sides of each of the two identical samples (labeled here as Sample A and Sample B).

A SEM image of the ellipsoidal Au particles on a glass substrate together with the transmittance of the particles for light with different directions of polarization is shown in Fig. 3.13. As expected, the particles exhibit a clear plasmonic resonance at a longer wavelength, around 1370 nm, when the incident light is linearly polarized in the direcion of the longer particle axis (polarization angle of 0°), and at a shorter wavelength, approximately 700 nm, when polarization is in the direction of the shorter particle axis (polarization angle of 90°). This is due to the transverse electronic oscillations that are induced in the direction of either semi-major axis of the particle, depending on the polarization. When the polarization direction is rotated to between 0° and 90°, a superposition of the modes of the two principal directions is formed, and thus the intensity of the plasmonic peak is reduced and the peak is broadened.

The emission measurements, presented in Figs. 3.14 and 3.15, show similar behavior. When polarization direction is 0°, the longer wavelength plasmonic resonance is excited, and the coupling efficiency exhibits a peak near the longer LSPR wavelength. When the polarization is rotated, the emission peak flattens,

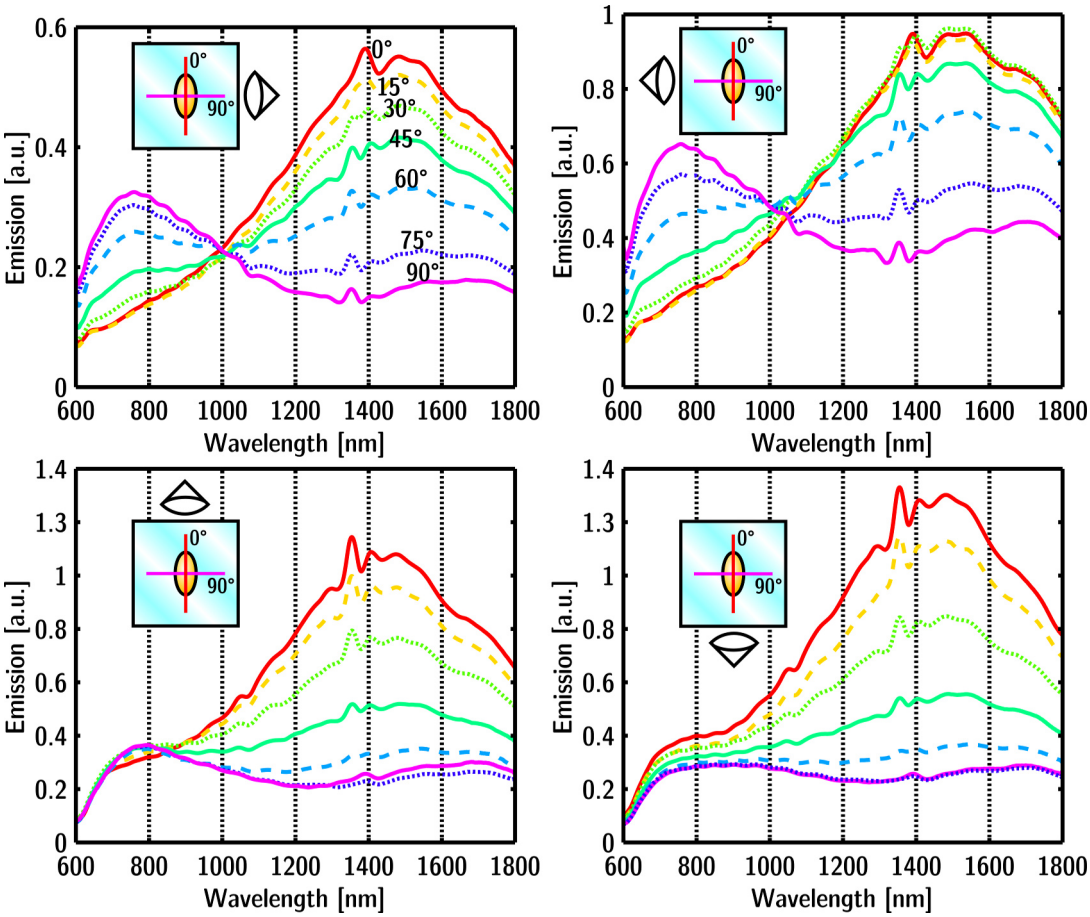

Figure 3.14: Emission out of the waveguide edge, measured from different sides of the Sample A with 42×200×400 nm (height × semi-minor axis × semi-major axis) ellipsoidal Au nanoparticles on a 1 mm thick glass. Insets on the graphs show the direction of polarization of the incident illumination with respect to the particle orientation, together with the direction of the emission measurement. Note the different scales on the graphs.

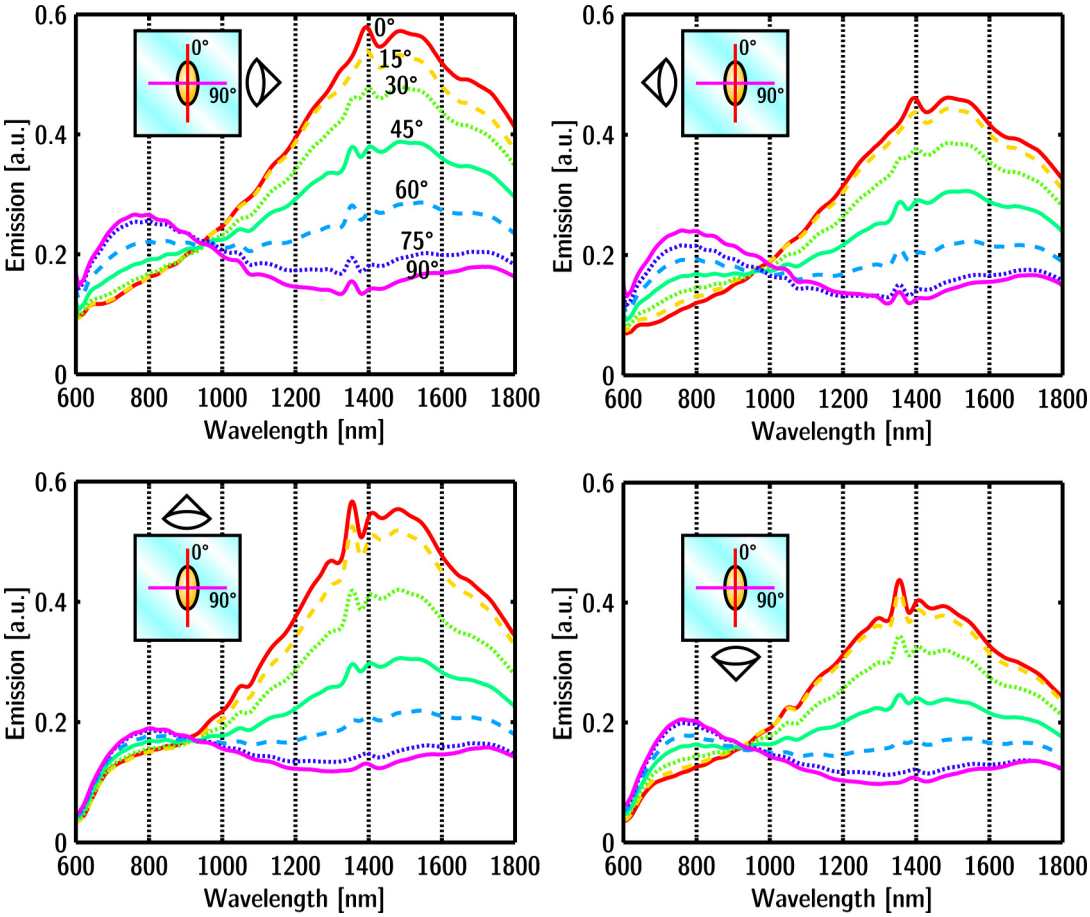

Figure 3.15: Emission out of the waveguide edge, measured from different sides of the Sample B with 42×200×400 nm (height × semi-minor axis × semi-major axis) ellipsoidal Au nanoparticles on a 1 mm thick glassInsets on the graphs show the direction of polarization of the incident illumination with respect to the particle orientation, together with the direction of the emission measurement.

and when approaching 90°, the emission peak appears near the shorter LSPR wavelength. This is due to the fact that the particles scatter into the waveguide most efficiently at the resonant wavelengths associated with the different polarization directions, and the relative strength of the resonance at particular direction of polarization.

The radiation pattern of an oscillating electric dipole in free space, as well as at an interface of two semi-infinite media, has zeros at the direction of the dipole axis and maxima at the directions perpendicular to the dipole axis. The situation is different, however, when the dipole is located at the surface of a substrate that supports guided modes. While free-space radiation is restricted to transverse electromagnetic (TEM) field modes, a planar dielectric waveguide also supports transverse magnetic (TM) modes, in which the electric field has a component parallel to the direction of mode propagation, as shown in Chapter 2.2. Thus, dipolar plasmonic modes of the nanoparticles may scatter into guided modes propagating in any direction. This means that the emission spectra measured with a given polarization should look similar, regardless of the direction from which the spectrum was measured from, with respect to the sample orientation.

On the Sample A (Fig. 3.14), however, the emission spectra measured from the direction of the semi-major particle axis seem to lack the shorter wavelength LSPR peaks near 90° polarization almost completely, compared to those measured in the direction of the semi-minor axis. On the Sample B (Fig. 3.15) the situation is not so apparent, although the shorter wavelength LSPR peak is fairly flat in the emission spectrum measured from the "upper" side of the sample. On both samples there are also significant differences in the overall emission intensities between measurements from different sides. These variations in the intensity, however, originate most probably from differences in the particle density at different parts of the sample. It is also possible that the absence of the short wavelength LSPR peaks in some of the measurements is due to differences in the nanoparticle quality at different locations on the sample, although it is peculiar that the short walength resonances are always weaker in the emission spectra measured from the direction of the semi-major particle axis. However, we have not found a conclusive explanation for this so far.

4

Conclusions

In this thesis work, a concept of a window integrated solar concentrator, utilizing light-coupling into a planar dielectric waveguide via plasmonic nanoparticles, was examined. Fabrication of metallic nanoparticles was investigated in order to produce particles that exhibit LSPR at wavelengths just above the wavelength range of visible light. It was found that with metal island film evaporation, used widely in studies of plasmon enhanced solar cells, one cannot precisely control the particle size or shape. It is possible, however, to achieve wide plasmonic resonance at wavelengths longer than that of visible light, by increasing the deposition thickness. The resonance wavelength may be tuned further by over or undercoating the island film with a high-refractive-index material. Nonetheless, it was found preferable for the interests of this study to employ the hole-mask colloidal lithography (HCL) process for the fabrication of the plasmonic particles, as it allows highly precise control over the particle size, shape, orientation and, thus, the plasmonic resonance wavelength.

Most importantly, coupling of light into planar waveguides by plasmonic nanoparticles was studied by directly measuring the intensity of light emitted out of the waveguide edge, when sample was illuminated with normal incidence either from the front or rear. It was found that while the particles couple light with good efficiency into the waveguide, the emission from the waveguide edge is very weak. Investigation of absorptance revealed that the cause of low emission intensity is the absorption effect of the plasmonic nanoparticles, that is mediated by the waveguide; light that is coupled into the waveguide interacts with large numbers of particles as it propagates, and thus the particles ultimately absorb nearly all of the light. This presents a severe problem for the solar consentrator.

When the particles were deposited directly on a 1 mm thick glass slide, it was observed that most efficient light coupling into the waveguide occurs at the wavelengths corresponding to the plasmonic resonances of the particles. With particles on a glass slide coated with a thin TiO_2 film, however, the thin-film resonance significantly effects the coupling. This is most probably due to the effect of interference to the electric field that excites the plasmons. Furthermore, coupling efficiency was always higher when the samples were illuminated from the rear. This effect is also linked to the thin-film interference and is associated to the difference in the reflectance of the particle-waveguide system, between front and rear illumination; when the sample is illuminated from the rear, reflectance is lowered, while the transmittance remains the same, and the amount of light coupled into the waveguide is increased.

Measurements on samples with ellipsoidal nanoparticles confirmed that, for linearly polarized light, there are two principal resonant wavelengths, corresponding to transverse electronic oscillations in the directions of the principal particle axes. Furthermore, the direction of polarization of the incident light determines which of these resonant wavelengths is coupled most efficiently into the waveguide.

One possible path of investigation in the future could be the exploitation of heat generated within the plasmonic particles. Due to the waveguide effect, the effective absorption coefficient of the particles on the waveguiding substrate becomes very high. As the electromagnetic energy absorbed by the particles is transformed into heat, it would perhaps be possible to transfer this heat to the edges of the window glass pane by utilizing *e.g.* transparent high-thermal-conductivity ceramics or doped glass as the window material, with sufficient efficiency for water heating or collection of energy in other form from the edges of the glass.

References

[1] L. He, M. D. Musick, S. R. Nicewarner, F. G. Salinas, S. J. Benkovic, M. J. Natan, and C. D. Keating, "Colloidal Au-Enhanced Surface Plasmon Resonance for Ultrasensitive Detection of DNA Hybridization," *J. Am. Chem. Soc.*, vol. 122, no. 38, pp. 9071–9077, 2000.

[2] S. Zeng, K.-T. Yong, I. Roy, X.-Q. Dinh, X. Yu, and F. Luan, "A Review on Functionalized Gold Nanoparticles for Biosensing Applications," *Plasmonics*, vol. 6, pp. 491–506, Apr. 2011.

[3] H. Félix-Rivera and S. P. Hernández-Rivera, "Raman Spectroscopy Techniques for the Detection of Biological Samples in Suspensions and as Aerosol Particles: A Review," *Sens. Imaging*, vol. 13, pp. 1–25, Sept. 2011.

[4] E. Ozbay, "Plasmonics: merging photonics and electronics at nanoscale dimensions.," *Science*, vol. 311, pp. 189–93, Jan. 2006.

[5] D. K. Gramotnev and S. I. Bozhevolnyi, "Plasmonics beyond the diffraction limit," *Nat. Photon.*, vol. 4, no. 2, pp. 83–91, 2010.

[6] H. A. Atwater and A. Polman, "Plasmonics for improved photovoltaic devices," *Nat. Mater.*, vol. 9, pp. 205–213, Mar. 2010.

[7] C. F. Bohren and D. R. Huffman, *Absorption and Scattering of Light by Small Particles.* Wiley, 1st ed., 2004.

[8] N. W. Ashcroft and N. D. Mermin, *Solid State Physics.* Saunders College Publishing, 1st ed., 1976.

[9] S. A. Maier, *Plasmonics: Fundamentals and Applications.* Springer, 1st ed., 2007.

[10] L. Novotny and B. Hecht, *Principles of Nano-Optics.* Cambridge University Press, 2nd ed., 2012.

[11] P. B. Johnson and R. W. Christy, "Optical constants of the noble metals," *Phys. Rev. B*, vol. 6, pp. 4370–4379, 1972.

[12] C. Sönnichsen, T. Franzl, T. Wilk, G. von Plessen, and J. Feldmann, "Drastic Reduction of Plasmon Damping in Gold Nanorods," *Phys. Rev. Lett.*, vol. 88, pp. 1–4, Jan. 2002.

[13] K. Okamoto, *Fundamentals of Optical Waveguides.* Elsevier, 2nd ed., 2006.

[14] D. Redfield, "Multiple-pass thin-film silicon solar cell," *Appl. Phys. Lett.*, vol. 25, no. 11, p. 647, 1974.

[15] S. Hegedus and A. Luque, *Photovoltaic Science and Engineering.* Wiley, 2nd ed., 2011.

[16] P. Campbell and M. A. Green, "Light trapping properties of pyramidally textured surfaces," *J. Appl. Phys.*, vol. 62, no. 1, p. 243, 1987.

[17] M. A. Green, "Lambertian light trapping in textured solar cells and light-emitting diodes: analytical solutions," *Prog. Photovoltaics*, vol. 10, pp. 235–241, June 2002.

[18] S. E. Han and G. Chen, "Toward the Lambertian limit of light trapping in thin nanostructured silicon solar cells.," *Nano Lett.*, vol. 10, pp. 4692–6, Nov. 2010.

[19] H. R. Stuart and D. G. Hall, "Absorption enhancement in silicon-on-insulator waveguides using metal island films," *Appl. Phys. Lett.*, vol. 69, no. 16, pp. 2327–2329, 1996.

[20] H. R. Stuart and D. G. Hall, "Enhanced Dipole-Dipole Interaction between Elementary Radiators Near a Surface," *Phys. Rev. Lett.*, vol. 80, pp. 5663–5666, June 1998.

[21] H. R. Stuart and D. G. Hall, "Island size effects in nanoparticle-enhanced photodetectors," *Appl. Phys. Lett.*, vol. 73, no. 26, pp. 3815–3817, 1998.

[22] B. J. Soller and D. G. Hall, "Energy transfer at optical frequencies to silicon-based waveguiding structures.," *J. Opt. Soc. Am. A*, vol. 18, pp. 2577–84, Oct. 2001.

[23] B. J. Soller, H. R. Stuart, and D. G. Hall, "Energy transfer at optical frequencies to silicon-on-insulator structures.," *Opt. Lett.*, vol. 26, pp. 1421–3, Sept. 2001.

[24] B. J. Soller and D. G. Hall, "Scattering enhancement from an array of interacting dipoles near a planar waveguide," *J. Opt. Soc. Am. B*, vol. 19, p. 2437, Oct. 2002.

[25] D. Derkacs, S. H. Lim, P. Matheu, W. Mar, and E. T. Yu, "Improved performance of amorphous silicon solar cells via scattering from surface plasmon polaritons in nearby metallic nanoparticles," *Appl. Phys. Lett.*, vol. 89, no. 9, p. 093103, 2006.

[26] K. Catchpole and S. Pillai, "Surface plasmons for enhanced silicon light-emitting diodes and solar cells," *J. Lumin.*, vol. 121, pp. 315–318, Dec. 2006.

[27] K. R. Catchpole and S. Pillai, "Absorption enhancement due to scattering by dipoles into silicon waveguides," *J. Appl. Phys.*, vol. 100, no. 4, p. 044504, 2006.

[28] S. Pillai, K. R. Catchpole, T. Trupke, G. Zhang, J. Zhao, and M. a. Green, "Enhanced emission from Si-based light-emitting diodes using surface plasmons," *Appl. Phys. Lett.*, vol. 88, no. 16, p. 161102, 2006.

[29] S. Pillai, K. R. Catchpole, T. Trupke, and M. a. Green, "Surface plasmon enhanced silicon solar cells," *J. Appl. Phys.*, vol. 101, no. 9, p. 093105, 2007.

[30] J. Mertz, "Radiative absorption, fluorescence, and scattering of a classical dipole near a lossless interface: a unified description,," *J. Opt. Soc. Am. B*, vol. 17, no. 11, pp. 1906–1913, 2000.

[31] S. P. Sundararajan, N. K. Grady, N. Mirin, and N. J. Halas, "Nanoparticle-induced enhancement and suppression of photocurrent in a silicon photodiode.," *Nano Lett.*, vol. 8, pp. 624–30, Feb. 2008.

[32] S. H. Lim, W. Mar, P. Matheu, D. Derkacs, and E. T. Yu, "Photocurrent spectroscopy of optical absorption enhancement in silicon photodiodes via scattering from surface plasmon polaritons in gold nanoparticles," *J. Appl. Phys.*, vol. 101, no. 10, p. 104309, 2007.

[33] F. J. Beck, A. Polman, and K. R. Catchpole, "Tunable light trapping for solar cells using localized surface plasmons," *J. Appl. Phys.*, vol. 105, no. 11, p. 114310, 2009.

[34] F. J. Beck, S. Mokkapati, a. Polman, and K. R. Catchpole, "Asymmetry in photocurrent enhancement by plasmonic nanoparticle arrays located on

the front or on the rear of solar cells," *Appl. Phys. Lett.*, vol. 96, no. 3, p. 033113, 2010.

[35] W. Liu, X. Wang, Y. Li, Z. Geng, F. Yang, and J. Li, "Surface plasmon enhanced GaAs thin film solar cells," *Sol. Energy Mater. Sol. Cells*, vol. 95, pp. 693–698, Feb. 2011.

[36] Z. Ouyang, X. Zhao, S. Varlamov, Y. Tao, J. Wong, and S. Pillai *Prog. Photovoltaics.*

[37] Z. Ouyang, S. Pillai, F. J. Beck, O. Kunz, S. Varlamov, K. R. Catchpole, P. Campbell, and M. A. Green, "Effective light trapping in polycrystalline silicon thin-film solar cells by means of rear localized surface plasmons," *Appl. Phys. Lett.*, vol. 96, no. 26, p. 261109, 2010.

[38] S. Pillai, F. J. Beck, K. R. Catchpole, Z. Ouyang, and M. A. Green, "The effect of dielectric spacer thickness on surface plasmon enhanced solar cells for front and rear side depositions," *J. Appl. Phys.*, vol. 109, no. 7, p. 073105, 2011.

[39] A. Goetzberger and W. Greubel, "Solar Energy Conversion with Fluorescent Collectors," *Appl. Phys.*, vol. 14, pp. 123–139, 1977.

[40] J. S. Batchelder, A. H. Zewail, and T. Cole, "Luminescent solar concentrators. 1: Theory of operation and techniques for performance evaluation.," *Appl. Opt.*, vol. 18, pp. 3090–110, Sept. 1979.

[41] J. S. Batchelder, A. H. Zewail, and T. Cole, "Luminescent solar concentrators. 2: Experimental and theoretical analysis of their possible efficiencies.," *Appl. Opt.*, vol. 20, pp. 3733–54, Nov. 1981.

[42] M. J. Currie, J. K. Mapel, T. D. Heidel, S. Goffri, and M. A. Baldo, "High-Efficiency Organic Solar Concentrators for Photovoltaics," *Science*, vol. 321, pp. 226–228, 2008.

[43] NREL, "Reference Solar Spectral Irradiance: Air Mass 1.5." `http://rredc.nrel.gov/solar/spectra/am1.5/`. [Online; accessed 10-June-2013].

[44] T. Bååk, "Silicon oxynitride; a material for GRIN optics," *Appl. Opt.*, vol. 21, no. 6, pp. 1069–1071, 1982.

[45] H. Fredriksson, Y. Alaverdyan, A. Dmitriev, C. Langhammer, D. S. Sutherland, M. Zäch, and B. Kasemo, "Hole–Mask Colloidal Lithography," *Adv. Mater.*, vol. 19, pp. 4297–4302, Dec. 2007.

[46] G. Xu, M. Tazawa, P. Jin, S. Nakao, and K. Yoshimura, "Wavelength tuning of surface plasmon resonance using dielectric layers on silver island films," *Appl. Phys. Lett.*, vol. 82, no. 22, pp. 3811–3813, 2003.

[47] F. J. Beck, E. Verhagen, S. Mokkapati, A. Polman, and K. R. Catchpole, "Resonant SPP modes supported by discrete metal nanoparticles on high-index substrates.," *Opt. Express*, vol. 19, pp. A146–56, Mar. 2011.

[48] K. R. Catchpole and A. Polman, "Plasmonic solar cells.," *Opt. Express*, vol. 16, pp. 21793–800, Dec. 2008.

A

Included publication

Direct optical measurement of light coupling into planar waveguide by plasmonic nanoparticles
Antti M. Pennanen and J. Jussi Toppari, Opt. Express 21, A23-A35 (2013)
http://www.opticsinfobase.org/oe/abstract.cfm?URI=oe-21-S1-A23

Direct optical measurement of light coupling into planar waveguide by plasmonic nanoparticles

Antti M. Pennanen* and J. Jussi Toppari

Department of Physics, Nanoscience Center, University of Jyväskylä, FIN-40014 Jyväskylä, Finland

**antti.m.pennanen@jyu.fi*

Abstract: Coupling of light into a thin layer of high refractive index material by plasmonic nanoparticles has been widely studied for application in photovoltaic devices, such as thin-film solar cells. In numerous studies this coupling has been investigated through measurement of *e.g.* quantum efficiency or photocurrent enhancement. Here we present a direct optical measurement of light coupling into a waveguide by plasmonic nanoparticles. We investigate the coupling efficiency into the guided modes within the waveguide by illuminating the surface of a sample, consisting of a glass slide coated with a high refractive index planar waveguide and plasmonic nanoparticles, while directly measuring the intensity of the light emitted out of the waveguide edge. These experiments were complemented by transmittance and reflectance measurements. We show that the light coupling is strongly affected by thin-film interference, localized surface plasmon resonances of the nanoparticles and the illumination direction (front or rear).

© 2012 Optical Society of America

OCIS codes: (240.6680) Surface plasmons; (000.2190) Experimental physics; (350.6050) Solar energy.

References

1. H. R. Stuart and D. G. Hall, "Absorption enhancement in silicon-on-insulator waveguides using metal island films," Appl. Phys. Lett. **69**, 2327–2329 (1996).
2. H. R. Stuart and D. G. Hall, "Enhanced dipole-dipole interaction between elementary radiators near a surface," Phys. Rev. Lett. **80**, 5663–5666 (1998).
3. H. R. Stuart and D. G. Hall, "Island size effects in nanoparticle-enhanced photodetectors," Appl. Phys. Lett. **73**, 3815–3817 (1998).
4. D. M. Schaadt, B. Feng, and E. T. Yu, "Enhanced semiconductor optical absorption via surface plasmon excitation in metal nanoparticles," Appl. Phys. Lett. **86**, 063106 (2005).
5. S. P. Sundararajan, N. K. Grady, N. Mirin, and N. J. Halas, "Nanoparticle-induced enhancement and suppression of photocurrent in a silicon photodiode," Nano Lett. **8**, 624–30 (2008).
6. H. A. Atwater and A. Polman, "Plasmonics for improved photovoltaic devices," Nat. Mater. **9**, 205–213 (2010).
7. S. Pillai, K. R. Catchpole, T. Trupke, G. Zhang, J. Zhao, and M. A. Green, "Enhanced emission from Si-based light-emitting diodes using surface plasmons," Appl. Phys. Lett. **88**, 161102 (2006).
8. K. R. Catchpole and S. Pillai, "Surface plasmons for enhanced silicon light-emitting diodes and solar cells," J. Lumin. **121**, 315–318 (2006).
9. D. Derkacs, S. H. Lim, P. Matheu, W. Mar, and E. T. Yu, "Improved performance of amorphous silicon solar cells via scattering from surface plasmon polaritons in nearby metallic nanoparticles," Appl. Phys. Lett. **89**, 093103 (2006).
10. S. Pillai, K. R. Catchpole, T. Trupke, and M. A. Green, "Surface plasmon enhanced silicon solar cells," J. Appl. Phys. **101**, 1–8 (2007).

11. S. H. Lim, W. Mar, P. Matheu, D. Derkacs, and E. T. Yu, "Photocurrent spectroscopy of optical absorption enhancement in silicon photodiodes via scattering from surface plasmon polaritons in gold nanoparticles," J. Appl. Phys. **101**, 104309 (2007).
12. K. R. Catchpole and A. Polman, "Plasmonic solar cells," Opt. Express **16**, 21793–800 (2008).
13. K. R. Catchpole and A. Polman, "Design principles for particle plasmon enhanced solar cells," Appl. Phys. Lett. **93**, 191113 (2008).
14. C. Hägglund, M. Zäch, G. Petersson, and B. Kasemo, "Electromagnetic coupling of light into a silicon solar cell by nanodisk plasmons," Appl. Phys. Lett. **92**, 053110 (2008).
15. K. Nakayama, K. Tanabe, and H. A. Atwater, "Plasmonic nanoparticle enhanced light absorption in GaAs solar cells," Appl. Phys. Lett. **93**, 121904 (2008).
16. Y. A. Akimov, W. S. Koh, and K. Ostrikov, "Enhancement of optical absorption in thin-film solar cells through the excitation of higher-order nanoparticle plasmon modes," Opt. Express **17**, 10195–205 (2009).
17. F. J. Beck, A. Polman, and K. R. Catchpole, "Tunable light trapping for solar cells using localized surface plasmons," J. Appl. Phys. **105**, 114310 (2009).
18. S. Mokkapati, F. J. Beck, A. Polman, and K. R. Catchpole, "Designing periodic arrays of metal nanoparticles for light-trapping applications in solar cells," Appl. Phys. Lett. **95**, 053115 (2009).
19. T. L. Temple, G. D. K. Mahanama, H. S. Reehal, and D. M. Bagnall, "Influence of localized surface plasmon excitation in silver nanoparticles on the performance of silicon solar cells," Sol. Energy Mater. Sol. Cells **93**, 1978–1985 (2009).
20. F. J. Beck, S. Mokkapati, A. Polman, and K. R. Catchpole, "Asymmetry in photocurrent enhancement by plasmonic nanoparticle arrays located on the front or on the rear of solar cells," Appl. Phys. Lett. **96**, 1–3 (2010).
21. Z. Ouyang, S. Pillai, F. J. Beck, O. Kunz, S. Varlamov, K. R. Catchpole, P. Campbell, and M. A. Green, "Effective light trapping in polycrystalline silicon thin-film solar cells by means of rear localized surface plasmons," Appl. Phys. Lett. **96**, 261109 (2010).
22. F.-J. Tsai, J.-Y. Wang, J.-J. Huang, Y.-W. Kiang, and C. C. Yang, "Absorption enhancement of an amorphous Si solar cell through surface plasmon-induced scattering with metal nanoparticles," Opt. Express **18**, A207–20 (2010).
23. F. J. Beck, E. Verhagen, S. Mokkapati, A. Polman, and K. R. Catchpole, "Resonant SPP modes supported by discrete metal nanoparticles on high-index substrates," Opt. Express **19**, A146–56 (2011).
24. W. Liu, X. Wang, Y. Li, Z. Geng, F. Yang, and J. Li, "Surface plasmon enhanced GaAs thin film solar cells," Sol. Energy Mater. Sol. Cells **95**, 693–698 (2011).
25. S. Mokkapati, F. J. Beck, R. de Waele, A. Polman, and K. R. Catchpole, "Resonant nano-antennas for light trapping in plasmonic solar cells," J. Phys. D: Appl. Phys. **44**, 185101 (2011).
26. Z. Ouyang, X. Zhao, S. Varlamov, Y. Tao, J. Wong, and S. Pillai, "Nanoparticle-enhanced light trapping in thin-film silicon solar cells," Prog. Photovolt: Res. Appl. **19**, 917–926 (2011).
27. S. Pillai, F. J. Beck, K. R. Catchpole, Z. Ouyang, and M. A. Green, "The effect of dielectric spacer thickness on surface plasmon enhanced solar cells for front and rear side depositions," J. Appl. Phys. **109**, 073105 (2011).
28. A. Paris, A. Vaccari, A. Calà Lesina, E. Serra, and L. Calliari, "Plasmonic scattering by metal nanoparticles for solar cells," plasmonics (2012).
29. T. F. Villesen, C. Uhrenfeldt, B. Johansen, J. L. Hansen, H. U. Ulriksen, and A. N. Larsen, "Aluminum nanoparticles for plasmon-improved coupling of light into silicon," Nanotechnology **23**, 085202 (2012).
30. Y. Yang, S. Pillai, H. Mehrvarz, H. Kampwerth, A. Ho-Baillie, and M. A. Green, "Enhanced light trapping for high efficiency crystalline solar cells by the application of rear surface plasmons," Sol. Energy Mater. Sol. Cells **101**, 217–226 (2012).
31. H. Fredriksson, Y. Alaverdyan, A. Dmitriev, C. Langhammer, D. S. Sutherland, M. Zäch, and B. Kasemo, "Hole–mask colloidal lithography," Adv. Mater. **19**, 4297–4302 (2007).

1. Introduction

Localized surface plasmons (LSPs) on metallic nanoparticles have since the beginning of this millennium been considered for enhancement of the efficiency of photovoltaic devices such as photodetectors [1–6], light emitting diodes [7] and, perhaps most importantly, solar cells [4–6, 8–30]. Two principal mechanisms for enhancement of the efficiency of solar cells by plasmonic particles have been identified [6]: (i) improved charge carrier generation caused by the near field of LSPs on metal nanoparticles embedded in photovoltaic material, and (ii) light trapping via scattering of light by LSPs on nanoparticles located on the front or rear surface of a solar cell. The latter has been proven to enhance the efficiency of thin-film solar cells, made of silicon (Si) [8–10, 17, 21, 26, 27] as well as other photovoltaic materials, such as gallium-arsenide (GaAs) [15, 24], by coupling light into the guided modes of the substrate, which is

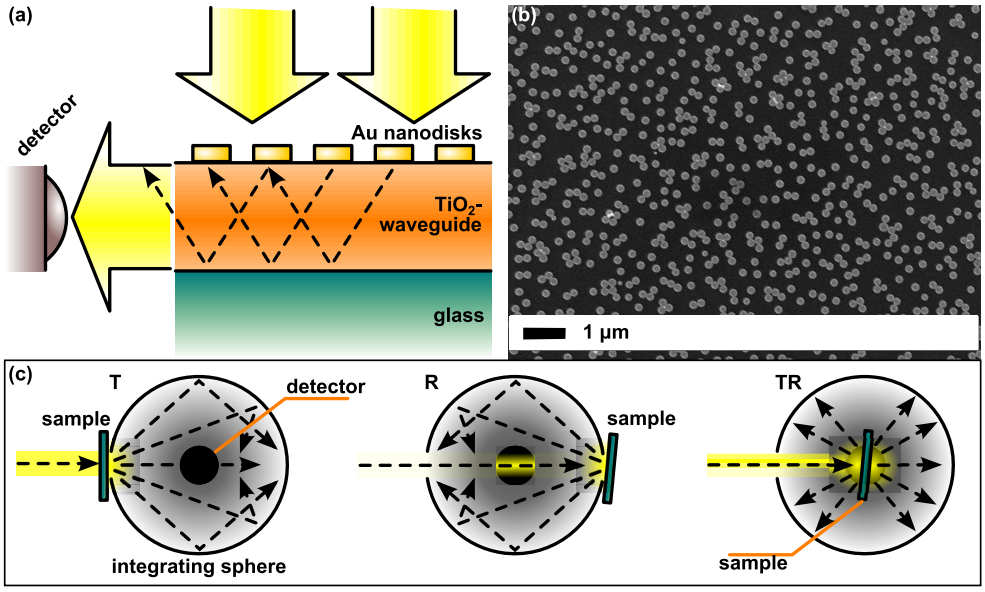

Fig. 1. (a) Illustration of the optical measurement geometry in the front illumination configuration. (b) SEM image of the 42 nm × 200 nm (height × diameter) Au nanodisks on a TiO_2-coated glass slide. (c) Measurement of total transmittance (T), reflectance (R) and transflectance (TR) with an integrating sphere. All transmitted/reflected light entering the integrating sphere is eventually collected into the detector, situated at the bottom of the sphere.

also the focus of this article. Light trapping and coupling of light into solar cell has been widely investigated by computational studies and by measuring the enhancement of the photocurrent or the quantum efficiency caused by nanoparticles. But, to our knowledge, up to this day, direct optical measurement of light coupling into the guided modes within a waveguide has not been conducted. Here we present such measurement.

2. Methods

2.1. Sample fabrication

Samples consisted of gold (Au) nanodisks deposited either directly on a 1 mm thick soda-lime glass substrate or a glass substrate coated with a thin layer of titanium dioxide (TiO_2), as illustrated in Fig. 1(a). TiO_2 layers, acting as a planar 2D-waveguides, with thickness ranging from 100 to 900 nm were grown on the glass substrates by atomic layer deposition (ALD). Samples were then cut to approximately 2×2 cm^2 size. Nanoparticle coatings of random arrays of circular gold nanodisks with height of 42 nm and diameter of 200 nm were fabricated by hole-mask colloidal lithography (HCL) [31]. Surface coverage of the particles was on average $(21 \pm 1)\%$. A scanning electron microscope (SEM) image of the Au particles on a TiO_2-coated glass slide is presented in Fig. 1(b). Compared to other easily fabricable shapes, such as spheres, nanodisks have high coupling efficiency to substrate [13, 23]. Gold was selected as preferred particle material because of its stability compared to for example silver, despite its higher absorption losses and slightly lower scattering cross-section. TiO_2 was used as the waveguide material because of its high refractive index and low optical absorption, to enable direct optical measurement of the waveguide coupling.

2.2. *Measurements*

The measurement geometry for investigation of the coupling efficiency is illustrated in Fig. 1(a). A broadband light source was used to illuminate the sample through a monochromator. Incident light is coupled into the waveguide by the nanoparticles and light emitted out of the waveguide edge is measured by photodiode. Measurements performed with this geometry will henceforth be referred to as emission measurements. We use the relative intensity of the emitted light compared to the incident intensity as a measure of coupling efficiency into the guided modes of the waveguide. It should be emphasized that by coupling efficiency we mean here the fraction of all light incident to sample surface that is coupled into the guided modes of the waveguide by the particles, in contrast to some references, where coupling efficiency is defined as the fraction of light scattered by particles that is scattered into the substrate. These emission measurements were carried out in two different configurations: the front illumination and the rear ilumination configuration. The front illumination configuration, where the sample is illuminated from the particle-coated side, is presented in Fig. 1(a). In the rear illumination configuration light is incident from the opposite side of the sample, *i.e.* substrate side, but otherwise the geometry remains the same as in Fig. 1(a).

An Oriel model 66182 light source with an USHIO halogen projector lamp was used for sample illumination, together with Acton SP2150 monochromator equipped with a 750 grooves/mm grating. Emission was measured with a Thorlabs PDA30G-EC AC-coupled amplified PbS photodiode (PD). To eliminate noise from the measurement we used an optical fork chopper in front of the monochromator entrance slit and a lock-in amplifier with the photodetector. Furthermore, a custom made slit with gold coated blades was installed into the front collar of the PD and sample edge was squeezed between the blades to exclude any external light from measurement and to efficiently collect the light emitted out of the waveguide edge by reflection from the gold coated inner surfaces of the blades. To eliminate higher order reflections from the illuminating light beam, long-pass filters with cut-off wavelengths of 600 and 1200 nm were used at the entrance of the monochromator.

To study the extinction and plasmonic properties of the particles, measurements of beam transmittance were performed on the samples with the equipment described above. The PD was placed behind the sample, on the path of the illumination beam.

Total (beam plus diffuse) transmittance and reflectance, as well as total transflectance measurements, were carried out with a dual beam Perkin Elmer Lambda 1050 UV-Vis-NIR spectrophotometer equipped with an integrating sphere accessory. These measurements are illustrated in Fig. 1(c). In transmittance measurements the sample was placed at the entrance port of the integrating sphere and the light transmitted through the sample was collected by the sphere into the detector. For reflectance measurements the sample was placed behind the sphere, at the reflectance measurement port, deflected 8 degrees from normal incidence angle, and the reflected light was collected by the sphere. Transflectance measurements were carried out by inserting the sample into the sphere by using center sample mount, deflected 8 degrees from normal incidence angle, allowing both transmitted and reflected light to be collected into the detector by the integrating sphere.

3. Results

3.1. *Emission measurements*

Bottom part of Fig. 2 shows measured transmittances of samples with Au disks on plain glass and on 100, 450 and 900 nm thick TiO_2 waveguides. The random particle arrays exhibit two discrete LSP resonances; the one on shorter wavelength is situated just under 700 nm for the particles on plain glass substrate and is red shifted to around 850 nm for particles on high

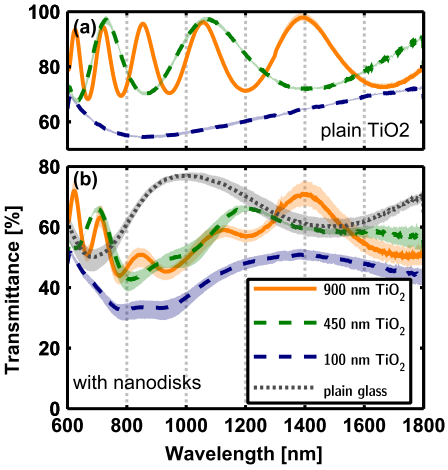

Fig. 2. (a) Transmittances of TiO_2 films without Au nanodisks and (b) transmission spectra of samples with nanoparticles on plain glass and on 900, 450 and 100 nm TiO_2. Bands around lines show the maximum error limits of measurements

refractive index TiO_2 substrate ($n \approx 2.3$), and the other one on longer wavelength at around 1450 nm for particles on plain glass and above 1800 nm for particles on TiO_2. In the transmission spectra of samples with TiO_2, the effect of thin-film interference may clearly be observed. In 450 and 900 nm films the effect is more noticeable, whereas in 100 nm film the variation as a function of wavelength is very slow and the effect, therefore, is not so prominent. Thin-film interference of plain TiO_2 films without nanoparticles is shown in top part of Fig. 2. All transmittances shown in Fig. 2 are averages of three separate measurements of different samples with similar coatings (particles and/or waveguide layer).

In the emission measurements, the intensity of the light emitted out of the waveguide edge was observed to be very low; less than 1% of the intensity of the beam illuminating the sample surface. This is attributed to cumulated absorption in the nanoparticles, which causes attenuation of the light propagating in the waveguide. Figures 3(a-d) illustrate the coupling of light into waveguides by the plasmonic particles, *i.e.* the intensity of light emitted out of the sample edge, in the direct optical measurement arrangement shown in Fig. 1. All emission spectra are averages of total of 9 to 12 separate measurements of three different samples with similar coatings. All emissions are normalized with the spectrum of the light source, which was measured with the same monochromator and detector as the emission from the sample edge. Figure 3(a) has the Au nanodisks directly on top of a plain glass substrate and Fig. 3(b-c) on top of 900, 450 or 100 nm thick TiO_2 waveguide layer, respectively. Emissions under front and rear illumination are shown.

The 1 mm thick glass substrate also itself acts as a waveguide for the light scattered by the Au particles, as may be observed from Fig. 3(a). The glass slide acts as a waveguide also when an additional high refractive index waveguide layer is present. Particles directly on a glass substrate exhibit largest coupling efficiencies near the surface plasmon resonance wavelengths, as do the samples with 100 nm TiO_2, for both front and rear illumination configurations.

For samples with 900 and 450 nm thick waveguides, however, the effect of thin-film interference begins to add complexity to the emission spectra. For the front illumination configuration the coupling is most efficient at the wavelengths corresponding to a constructive thin-film interference in the transmittance spectra. Emission spectra of samples with 900 nm TiO_2 films

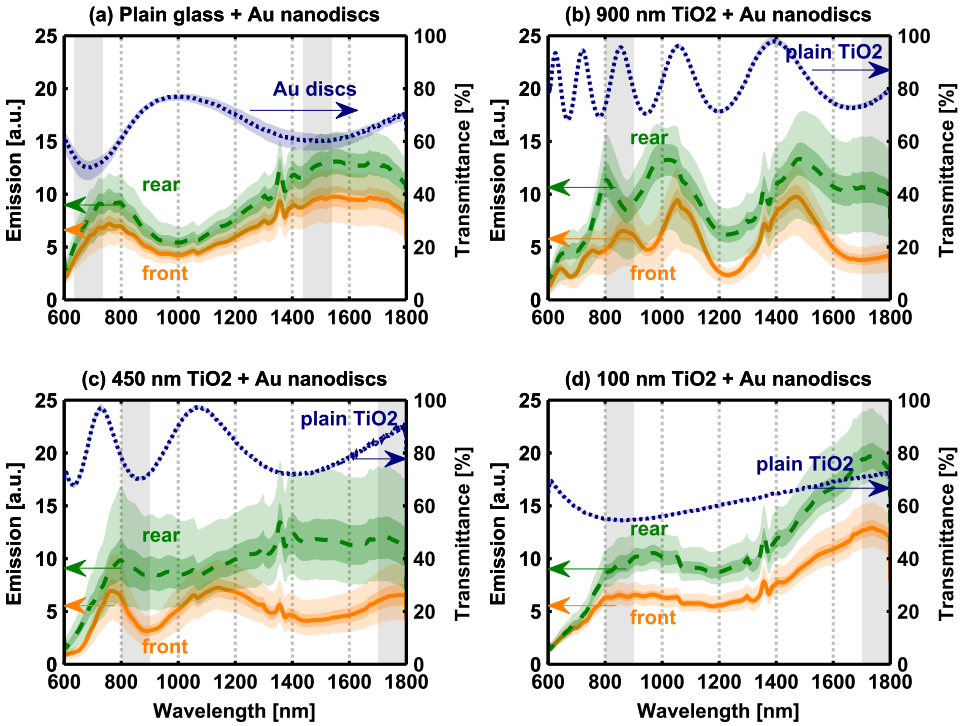

Fig. 3. Emission spectra, *i.e.* intensity of light emitted out of the waveguide edge in front (solid orange line) and rear (dashed green line) illumination configurations, of samples with Au nanodisks on (a) plain glass and (b) 900, (c) 450 and (d) 100 nm TiO_2. Dotted lines: Transmittance of the Au particles on glass is shown for reference in (a) and transmittance of the TiO_2 films without the nanoparticles in (b–d), to illustrate the correspondence between thin-film interference and coupling efficiency. Bands around lines show the 95 % confidence bands (inner bands) and maximum errors (outer bands) of measurements. If only one band is visible, it is the maximum error band. Vertical bands show locations of the resonant LSP modes.

show some interference-like pattern in the rear illumination configuration also, but the number and positions of the emission peaks are different to the measurement with front illumination. Samples with 450 nm waveguides do not show interference pattern in the emission spectrum under rear illumination.

Effect of a spacer layer on the coupling efficiency was investigated by adding an ALD deposited 50 nm thick aluminum oxide (Al_2O_3) layer between the particles and the 900 nm TiO_2 waveguide (Fig. 4). Refractive index of the Al_2O_3 film is $n \approx 1.6$. The spacer layer of 50 nm is thick enough to substantially shift the localized surface plasmon resonances of the Au nanodisks (Fig. 4(a)), but causes significantly smaller shift in thin-film interference maxima and minima (Fig. 4(b)).

With front illumination the coupling efficiency into the guided modes of the waveguide is increased or decreased on different wavelengths when spacer layer is added, but there is no noticeable overall increase or decrease. When illuminated from rear, there is a net decrease in coupling efficiency, with addition of the spacer layer. These results are in agreement with those presented in previous studies [20, 21, 23, 27, 30].

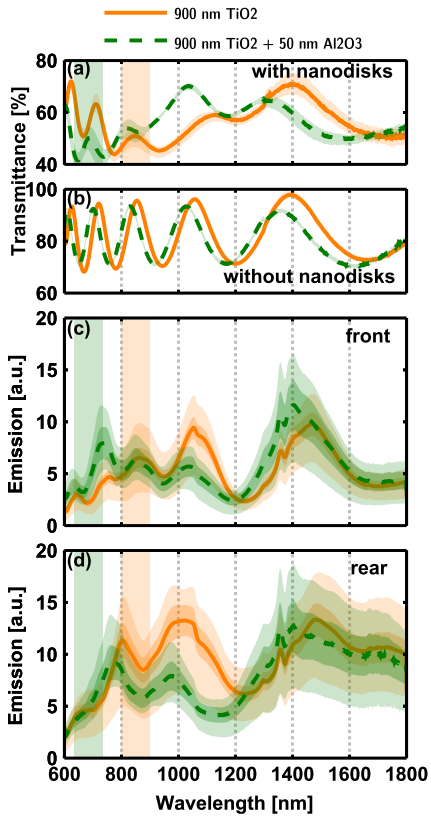

Fig. 4. Effect of spacer layer on the coupling efficiency. Samples with 900 nm TiO_2 waveguide and Au nanodisks with (dashed green lines) and without (solid orange lines) the spacer layer. (a) Transmittances. (b) Transmittances without the nanodisks. (c,d) Emission spectra under front and rear illumination, respectively. Bands around lines show the 95 % confidence bands (inner bands) and maximum errors (outer bands) of measurements. If only one band is visible, it is the maximum error band. Vertical bands show the locations of the shorter wavelength LSP resonances.

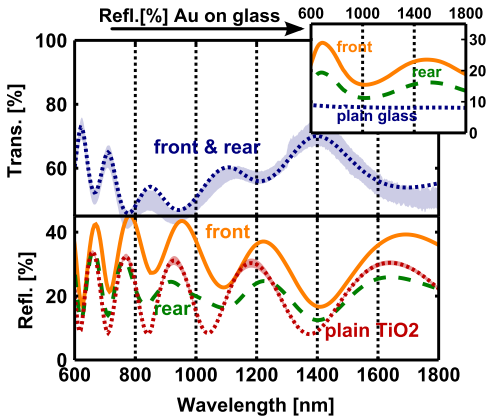

Fig. 5. Sample with 900 nm TiO_2 and Au nanodisks. Upper part: total transmittance (dotted blue line) and beam transmittance with maximum error limits (band around dotted line). Lower part: Total reflectance for front (solid orange line) and rear illumination (dashed green line) and for sample without Au nanodisks (dotted red line). Inset: total reflectance of Au nanodisks on plain glass.

3.2. Transmittance and reflectance measurements

In order to gain additional insight into the asymmetry in coupling efficiency between front and rear illumination, measurements with a dual-beam spectrophotometer and an integrating sphere were carried out. One individual sample with 900 nm TiO_2 waveguide and 42 $\times$ 200 nm circular Au disks was selected for these measurements. Results of the total transmittance and reflectance measurements, with both front and rear illumination, are shown in Fig. 5. Inset shows measured reflectances for Au nanodisks on plain glass for reference.

On plain glass, the Au nanodisks increase the reflectance, and reflectance is significantly larger for front than rear illumination. Au particles on TiO_2 coated glass increase the reflectance when the sample is illuminated from the front and cause the reflectance to increase or decrease, depending on the wavelength, when illuminated from the rear. In this respect our samples behave differently compared to Si solar cells, where nanoparticles act as an anti-reflection coating, when deposited on the front surface of the cell [10, 20, 27]. This difference is due to high transparency of the glass/TiO_2 substrate which is always decreased by addition of nanoparticles (for more deatailed discussion, see section 4.3). On TiO_2 coated glass, the transmittance is essentially the same for both front and rear illumination. Beam transmittance of three individual samples is shown as a band around the total transmittance plot (from the one selected sample). In this case the total transmittance is essentially equal to the beam transmittance, *i.e.* the diffuse transmittance is negligible. The measured total reflectance of the plain TiO_2 film is shown for reference. Difference between front and rear reflectance of the plain TiO_2 sample is negligible.

Mechanisms behind the electro-magnetic coupling between the nanoparticles and waveguide modes are further investigated in Fig. 6. Absorption in the samples was calculated from the total reflectance and transmittance measurements as (Abs) = 100 %−((Trans)+(Refl)) and from the total transflectance measurements as (Abs) = 100 %−(Transfl). Absorption spectra in Fig. 6(a) show apparent similarity in shape and relative magnitude to the emission spectra in Fig. 6(b).

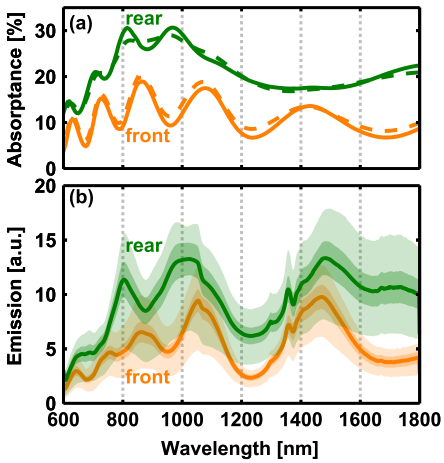

Fig. 6. (a) Absorption of sample with 900 nm TiO_2 and Au nanodisks. Solid lines: absorptance from the separate total transmittance and reflectance measurements; dashed lines: absorptance from the transflectance measurements. (b) Emission spectrum of same sample, same as in Fig. 3(b).

4. Discussion

4.1. Effect of plasmon resonance and thin-film interference

Au particles on plain glass substrate and on the thinnest 100 nm TiO_2 waveguide show largest coupling efficiency near the wavelengths of the localized surface plasmon resonances, with both front and rear illumination. The effect of the very thin TiO_2 waveguide is to red-shift the plasmon resonance (as can be observed from Fig. 2), and thus the peaks in coupling efficiency, and to increase the coupling efficiency near the second, longer wavelength plasmon resonance. Looking at the transmittance spectrum of plain 100 nm TiO_2 film, this is probably due to constructive thin-film interference near the longer localized surface plasmon resonance wavelength. What is notable here is that the 100 nm TiO_2 waveguide does not support guided modes at wavelengths above around 850 nm. Therefore, above this wavelength, all emission comes from the glass substrate acting as a waveguide. Emission enhancement from plain glass to 100 nm TiO_2 coated glass may be (at least partly) attributed to the change in dielectric environment of the particle: first, the particle scattering tends to be directed more strongly to the larger refractive index, and second, the scattering efficiency of the particle may be increased by the higher refractive index environment [12]. The presence of the very thin TiO_2 film may also direct the scattering into directions more preferable for the guided modes in the glass substrate, *i.e.* to angles more parallel to the waveguide.

With 900 and 450 nm TiO_2 films also the thin-film interference significantly affects the coupling efficiency. Based on the behaviour of the emission in samples with no or 100 nm TiO_2, it seems most plausible that the coupling is defined by the plasmon resonances but modified by the driving field, which is defined by the thin-film interference. It should be noted, that the thin-film interference effect does not manifest itself in heavily absorbing waveguides, where the optical path length is shorter than the device thickness. But even in Si or GaAs solar cells interference effects become significant when the cell thickness is low and at wavelengths where the optical absorption is weak, so that optical path lengths of several times the device thickness are required for efficient photocurrent generation at the corresponding wavelength. What is notable

here is that the coupling efficiency of incident light into the guided modes of the substrate is most prominently dependent on the thin-film interference and not, for example, the waveguide modes, contrary to what has been observed in some previous studies [2, 7].

4.2. Effects of near and far fields

In the emission spectra of Fig. 3, the short and long wavelength localized surface plasmon modes both contribute to the coupling of light into the waveguide. Some numerical studies [14, 23] suggest that for disk shaped metal nanoparticles on a high refractive index substrate, the discrete resonances at different wavelengths are associated with different field distributions. Beck *et al.* [23] observe two separate resonances in Ag disks; on shorter wavelengths the resonance is associated with modes localized at the particle-air interface, while the longer wavelength resonances involve modes at the particle-substrate interface. Hägglund *et al.* [14] argue that the coupling efficiency to waveguide is determined by the far field whereas Catchpole *et al.* [13] and Beck *et al.* [23] emphasize the importance of near-field coupling. We observe no significant difference in strength of the coupling to the waveguide between the shorter and longer wavelength plasmonic modes, even though according to Hägglund *et al.* [14] as well as Catchpole *at al.* [13] and Beck *at al.* [23] the near field localizations are completely different for the two resonances. Thus it seems that, as Hägglund *at al.* [14] suggested, the coupling into the waveguide is not affected by the different near field distributions associated with the individual plasmonic modes, but is determined by the far field.

Particles deposited on the front surface of a photovoltaic cell may enhance or suppress the photocurrent and efficiency of the device, depending on the wavelength. Suppression of the photocurrent and the decrease of efficiency of Si solar cells at just below LSP resonance wavelength, due to the destructive interference between incident and scattered fields, has been reported in many studies [5, 11, 17, 20, 24]. Furthermore, constructive or destructive interference may arise from different field distributions associated with the different resonant modes, causing either positive or negative effect on the solar cell efficiency [14]. In our measurements, the emission spectra suggest that coupling occurs also for wavelengths just below the first, shorter wavelength resonance, as well as the second, longer wavelength resonance. Effect of this coupling would be to increase the optical path length of photons and thus enhance photocurrent in photovoltaic material. However, the field scattered by the particles may be at opposite phase with the incident field, as suggested in numerous studies [5, 11, 17, 20, 24], causing decrease in field intensity near the particle. The net effect on the photocurrent generation may thus be negative, as observed in references mentioned above.

4.3. Asymmetry between front and rear illumination

Negative effects of destructive interference on solar cell efficiency may be avoided by placing the particles on the rear surface of the cell [17, 20, 21, 26, 27]. Placement of the particles to the rear of the cell also avoids the negative effect of particle absorption to the cell performance, compared to front deposition [8, 26]. Particles located on the rear surface of a thin-film Si cell have been reported to provide larger quantum efficiency enhancement than front located particles [17, 26]. In some references it is reported that there is no significant difference in the fraction of light scattered by the particles that is scattered into the substrate between front and rear located particles [20, 27], while there is a notable asymmetry in another reference [25]. These differences may be due to different particle sizes simulated in different references. In the measurements presented here the coupling efficiency to the guided modes within the waveguide, measured as the emission from the sample edge, is higher for rear illumination for all samples (see Fig. 3). Thus, it seems that for Au nanodisks used here, the fraction of incident light that is coupled into the guided modes of the substrate does depend on the illumination

direction. The difference in coupling efficiency to guided modes between front and rear illuminations observed in our measurements is larger for the samples with TiO_2, compared to that with just plain glass. This would suggest that the higher refractive index environment of the nanoparticles causes the asymmetry in coupling efficiency between front and rear illumination configurations to be increased. This interpretation is further supported by the measurements of the samples with a 50 nm Al_2O_3 spacer layer; in Fig. 4 asymmetry in the coupling efficiency is decreased when the lower refractive index Al_2O_3 spacer layer is introduced between the high index TiO_2 substrate and the nanoparticles.

To further investigate the asymmetry in the coupling efficiency, measurements of reflectance, transmittance and transflectance were conducted with an integrating sphere on one selected sample with 900 nm TiO_2 and Au nanodisks. In Fig. 5 total transmittances are equal in front and rear illumination. Total transmittance is also essentially equal to the beam transmittance, indicating that all transmittance is beam. This would suggest that the scattering into the forward direction by the particles is zero. Total reflectances, however, are different for front and rear illumination, implying that backward scattering is affected by the direction of illumination. This may be due to the asymmetry in refractive index around the particle, as the scattering tends to be directed towards the higher index. When illuminated from the rear, particles tend to scatter more efficiently into the backward direction, but this backscattered light is then coupled efficiently into the waveguide, resulting in the decrease of reflectance. This interpretation, however, does not explain the absence of forward scattering in the transmittance measurements.

In the emission measurements, the intensity of light emitted out of the waveguide edge was found to be very low. We attributed this to the cumulated absorption in the nanoparticles. This interpretation is supported by Fig. 6, where absorptance of the sample with 900 nm TiO_2 coating is 30 % at its highest for rear and 20 % for front illumination. The absorptance of plain 900 nm TiO_2 film is negligible. Furthermore, the features and relative magnitude of absorptances under front and rear illumination in Fig. 6(a) are similar to those of corresponding emission spectra in Fig. 6(b). This may be understood as follows: When light, trapped into the waveguide, propagates and interacts with the nanoparticles, an individual particle may interact with it by either absorption or scattering. Since the refractive index of the TiO_2 substrate is much higher than that of air, scattering is predominantly directed into the waveguide. But even if the particles scatter with much higher efficiency than they absorb, the light propagating in the waveguide interacts with very high number of particles, leading to significant absorption loss. There is thus a correspondence between the coupling efficiency and the sample absorptance. Since the transmittance is independent of the illumination direction, the asymmetry in absorptance and coupling efficiency between front and rear illumination is related to the asymmetry in reflectance, *i.e.* back scattering. This interpretation is illustrated in Fig. 7: transmission through the sample remains the same, regardless of the illumination direction, but the reflectance and the fraction of incident light coupled into the waveguide changes. What is notable here is that the front reflectance is higher than the rear reflectance: on Si cells, front located nanoparticles typically act as an antireflection coating, reducing the reflectance, but the antireflection property is absent for rear located particles [20]. In our measurements, the reflectance of the sample with Au disks is actually higher than that of plain TiO_2, as seen in Fig. 5. This is explained by the fact that in our samples the substrate and the waveguide are highly transparent, contrary to the Si solar cells, and thus the introduction of metal nanoparticles onto the sample surface decreases the transmittance. Under front illumination, this is observed as increased reflectance at all wavelengths. Together with decreased transmittance, the effect of the Au nanodisks is to couple incident light into the waveguide, leading to absorption losses. As observed in Fig. 3, this coupling is more efficient when illuminating the sample from rear, which explains the decrease in reflectance at some wavelengths and increase at others under rear illumination.

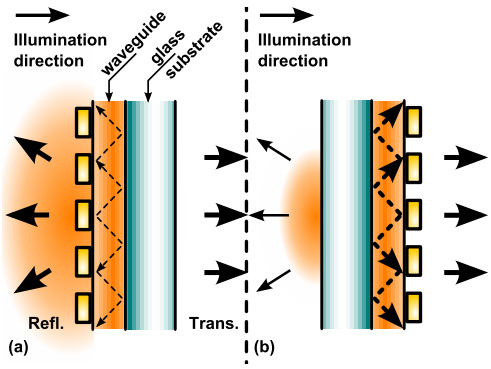

Fig. 7. Transmission and reflection illustrated with (a) front and (b) rear illumination. Reflectance is decreased when the sample is illuminated from the rear, whereas transmittance remains unchanged.

4.4. Effect of spacer layer

Addition of a 50 nm Al_2O_3 spacer layer between the particles and the high index waveguide causes a substantial blueshift to the resonances, but also a much smaller shift to the interference pattern in the transmittance of the bare TiO_2 film. The shift in the resonance peaks results in a shift of the enhancement peaks in the emission spectra for both front and rear illumination. The small shift in the thin-film interference pattern causes a small shift to the interference pattern of the emission spectra also. The most prominent effect of the addition of the spacer layer on the coupling efficiency in the front illumination configuration is to shift the position of the enhancement peaks, due to the blueshift of the plasmonic resonance. With rear illumination, however, the addition of the spacer layer results in noticeable decrease of emission at wavelengths of 800–1200 nm. Our measurements are in agreement with previous results [20, 26, 27] that rear located particles exhibit highest coupling efficiency when deposited directly on a high index substrate.

5. Conclusions

Here we present the first direct optical measurement of the coupling of light into a planar waveguide by plasmonic nanoparticles. As a conclusion, we have observed that if the high-index waveguide is situated on a transparent substrate or superstrate, the thin-film interference significantly affects the coupling between the particle plasmons and waveguide modes. This arises from the differences in strength of the electromagnetic field driving the particle plasmons, caused by the interference effects. These effects could be significant in thin-film photovoltaic cells at wavelengths near the band gap, where optical absorption is weak. It seems that the efficiency of light coupling into the guided modes is most importantly determined by the thin-film interference and the plasmon resonances, and not, for example, the waveguide modes, contrary to what has been reported in some previous studies. [2, 7] Au nanodisks used in this study exhibited two distinct localized plasmon resonances, both of which demonstrated coupling into the waveguide.

We have also noted that the coupling efficiency into the guided modes is different under front and rear illuminations, which is in agreement with results of other studies [17, 20, 25–27]. With no spacer layer, the coupling efficiency is greater for rear illumination, but addition of a 50 nm Al_2O_3 spacer layer decreases the efficiency in rear illumination configuration. The difference in the coupling efficiency between front and rear illumination is closely associated with the difference in the total reflectance of the nanoparticle-waveguide system.

Appendix A: Au nanodisk fabrication

In the HCL [31] process, the glass slides were first spin coated with 495 PMMA-A2 for 1 minute at 2000 rpm and baked for 10 mins at 170°C. The PMMA layer was then made hydrophilic by oxygen plasma treatment in reactive ion etch (RIE), with 50 W power for 5 seconds. Samples were then covered with 0.2 weight% PDDA (poly-diallyldimethylammonium chloride) solution for 30 secs, rinsed with de-ionized water for another 30 secs and dried by pressing gently with a clean room sheet; then covered for 2 mins with 0.2 wt% water solution of polystyrene (PS) nanospheres with 200 nm diameter, rinsed with DI water for 1 min and dried with a clean room sheet. Clean room sheets were used for drying instead of blowing with N_2 to prevent sedimentation of the PS particles on the relatively large sample surface. A mask layer was produced by first evaporating approximately 15 nm of Au under ultra high vacuum and then stripping off the PS nanospheres by transparent tape. The PMMA layer was etched through the mask by O_2 plasma in RIE for 1 min 12 secs with 50 W power. The nanoparticles were deposited by evaporating 42 nm of Au under ultra high vacuum. Lift-off procedure of the sacrificial PMMA layer was performed by ultrasonicating the samples for 5 mins in boiling acetone. Finally, the samples were rinsed with isopropanol and DI water and blown dry with N_2.

Acknowledgments

We would like to thank the Foundation for Research of Natural Resources in Finland (Suomen Luonnonvarain Tutkimussäätiö) for funding; J. Maula, Beneq for the ALD depositions; H. Tuovinen, University of Eastern Finland, Joensuu for arranging and J. Hiltunen, SIB-labs for conducting measurements with spectrophotometer and integrating sphere.